



# Parallels between retinal and brain pathology and response to immunotherapy in old, late-stage Alzheimer's disease mouse models

Jonah Doustar<sup>1</sup> | Altan Rentsendorj<sup>1</sup> | Tania Torbati<sup>1,2</sup> | Giovanna C. Regis<sup>1</sup> | Dieu-Trang Fuchs<sup>1</sup> | Julia Sheyn<sup>1</sup> | Nazanin Mirzaei<sup>1</sup> | Stuart L. Graham<sup>3,4</sup> | Prediman K. Shah<sup>5</sup> | Mitra Mastali<sup>6,7</sup> | Jennifer E. Van Eyk<sup>6,8,9</sup> | Keith L. Black<sup>1</sup> | Vivek K. Gupta<sup>10</sup> | Mehdi Mirzaei<sup>3,10,11</sup> | Yosef Koronyo<sup>1</sup> | Maya Koronyo-Hamaoui<sup>1,6</sup>

<sup>1</sup>Department of Neurosurgery, Cedars-Sinai Medical Center, Maxine Dunitz Neurosurgical Research Institute, Los Angeles, CA, USA

<sup>2</sup>College of Osteopathic Medicine of the Pacific, Western University of Health Sciences, Pomona, CA, USA

<sup>3</sup>Department of Clinical Medicine, Macquarie University, Sydney, NSW, Australia

<sup>4</sup>Save Sight Institute, Sydney University, Sydney, NSW, Australia

<sup>5</sup>Oppenheimer Atherosclerosis Research Center, Cedars-Sinai Heart Institute, Los Angeles, CA, USA

<sup>6</sup>Department of Biomedical Sciences, Cedars-Sinai Medical Center, Los Angeles, CA, USA

<sup>7</sup>Cedars-Sinai Medical Center, Smidt Heart Institute, Los Angeles, CA, USA

<sup>8</sup>Barbara Streisand Women's Heart Center, Cedars-Sinai Medical Center, Los Angeles, CA, USA

<sup>9</sup>Department of Medicine, Cedars-Sinai Medical Center, Los Angeles, CA, USA

<sup>10</sup>Department of Molecular Sciences, Macquarie University, Sydney, NSW, Australia

<sup>11</sup>Australian Proteome Analysis Facility, Macquarie University, Sydney, NSW, Australia

## Correspondence

Maya Koronyo-Hamaoui, Cedars-Sinai Medical Center, 127 S. San Vicente Blvd., Los Angeles, CA 90048, USA.  
Email: maya.koronyo@csmc.edu

## FUNDING INFORMATION

National Institute on Aging, Grant/Award Number: R01AG055865, R01AG056478; National Health and Medical Research Council; Australian Government's National Collaborative Research Infrastructure Scheme; The Saban Family Foundation; Tom Gordon Foundation; The Maurice Marciano Family Foundation; Macquarie University and Peterson Foundation.

## Abstract

Despite growing evidence for the characteristic signs of Alzheimer's disease (AD) in the neurosensory retina, our understanding of retina–brain relationships, especially at advanced disease stages and in response to therapy, is lacking. In transgenic models of AD (APP<sub>SWE</sub>/PS1<sub>ΔE9</sub>; ADtg mice), glatiramer acetate (GA) immunomodulation alleviates disease progression in pre- and early-symptomatic disease stages. Here, we explored the link between retinal and cerebral AD-related biomarkers, including response to GA immunization, in cohorts of old, late-stage ADtg mice. This aged model is considered more clinically relevant to the age-dependent disease. Levels of synaptotoxic amyloid  $\beta$ -protein (A $\beta$ )<sub>1–42</sub>, angiopathic A $\beta$ <sub>1–40</sub>, non-amyloidogenic A $\beta$ <sub>1–38</sub>, and A $\beta$ <sub>42</sub>/A $\beta$ <sub>40</sub> ratios tightly correlated between paired retinas derived from oculus sinister (OS) and oculus dexter (OD) eyes, and between left and right posterior brain hemispheres. We identified lateralization of A $\beta$  burden, with one-side dominance within paired retinal and brain tissues. Importantly, OS and OD retinal A $\beta$  levels correlated with their cerebral

Altan Rentsendorj, Tania Torbati and Giovanna C. Regis contributed equally to this study.

This is an open access article under the terms of the Creative Commons Attribution License, which permits use, distribution and reproduction in any medium, provided the original work is properly cited.

© 2020 The Authors. *Aging Cell* published by the Anatomical Society and John Wiley & Sons Ltd.



counterparts, with stronger contralateral correlations and following GA immunization. Moreover, immunomodulation in old ADtg mice brought about reductions in cerebral vascular and parenchymal A $\beta$  deposits, especially of large, dense-core plaques, and alleviation of microgliosis and astrocytosis. Immunization further enhanced cerebral recruitment of peripheral myeloid cells and synaptic preservation. Mass spectrometry analysis identified new parallels in retino-cerebral AD-related pathology and response to GA immunization, including restoration of homeostatic glutamine synthetase expression. Overall, our results illustrate the viability of immunomodulation-guided CNS repair in old AD model mice, while shedding light onto similar retino-cerebral responses to intervention, providing incentives to explore retinal AD biomarkers.

#### KEYWORDS

astrocytes reactivation, glutamine synthetase, myeloid cells, neurodegenerative disease, ocular proteins, retina, synaptic preservation, vascular amyloidosis

## 1 | INTRODUCTION

In recent years, a surge of studies have indicated that the pathological hallmarks of Alzheimer's disease (AD) extend beyond the brain and manifest in the retina of patients (Alexandrov et al., 2011; den Haan et al., 2018; Hadoux et al., 2019; Koronyo et al., 2017; Koronyo-Hamaoui et al., 2011; La Morgia et al., 2016; Schon et al., 2012; Schultz et al., 2020; Shi et al., 2020; Tsai et al., 2014). AD is a fatal neurodegenerative disorder and the most common form of dementia clinically diagnosed by the progressive loss of memory and cognitive function (Alzheimer's Association, 2018). Neuropathologically, AD is typified by progressive, age-dependent accumulation of amyloid  $\beta$ -protein (A $\beta$ ; Sperling et al., 2020) in both soluble and insoluble plaque conformations, as well as neurofibrillary tangles mostly comprised of hyperphosphorylated tau, leading to vast synaptic and neuronal degeneration (De Strooper & Karran, 2016; Hardy et al., 1998; Li et al., 2020). In particular, A $\beta_{42}$  and A $\beta_{40}$  alloforms have been strongly implicated in AD pathogenesis and cognitive decline (Benilova et al., 2012; Chiti & Dobson, 2017; Kaye et al., 2003; Lambert et al., 1998; McLean et al., 1999; Shankar et al., 2008). Neuroinflammation is another key component of the AD pathological continuum characterized by a marked presence of chronically activated microglia (microgliosis) and reactive astrocytes (astrocytosis) in the vicinity of A $\beta$  deposition. These are commonly viewed as detrimental immune responses in the AD brain and have been linked to synaptic loss and cognitive decline (Heneka et al., 2015; Wyss-Coray & Mucke, 2002).

To reduce amyloidosis and regulate neuroinflammation, various immunomodulatory strategies were investigated for their potential therapeutic impact in preclinical rodent models of AD (Bakalash et al., 2011; Bernstein et al., 2014; Butovsky et al., 2006, 2007; Frenkel et al., 2005; Koronyo et al., 2015; Koronyo-Hamaoui et al., 2009, 2011, 2014, 2020; Li et al., 2020; Rentsendorj et al., 2018; Rosenzweig et al., 2019). Many recent studies have demonstrated

beneficial effects of these immunomodulatory approaches in preventing, halting, or reversing AD pathologies and preserving memory and learning functions. Glatiramer acetate (GA; also termed Copaxone<sup>®</sup>), an FDA-approved drug used for the treatment of relapsing-remitting multiple sclerosis, has displayed promising results in young and adult double-transgenic APP<sub>SWE</sub>/PS1 $\Delta$ E9 (ADtg) mice. A $\beta$  burden, astrocytosis, and microgliosis were diminished, brain milieu shifted from a pro- to anti-inflammatory profile, synapses were rescued, and hippocampal neurogenesis was induced, ultimately preventing cognitive decline (Bakalash et al., 2011; Baruch et al., 2015; Butovsky et al., 2006, 2007; Frenkel et al., 2005; Koronyo et al., 2012, 2015; Rentsendorj et al., 2018). The therapeutic mechanisms of GA immunization, mainly explored in these transgenic AD model mice (Butovsky et al., 2006, 2007; Koronyo et al., 2012, 2015; Rentsendorj et al., 2018), were attributed to a shift in microglial phenotype and enhanced recruitment of neuroprotective, peripherally derived monocytes and macrophages directly involved in A $\beta$  clearance, immunoregulation, and neuroregeneration (Koronyo et al., 2015; Rentsendorj et al., 2018). While these promising effects were reported in pre- and early-symptomatic (5- to 12-month-old) ADtg mice, they have never been investigated in old, late-stage mouse models of AD. Given that aging is a fundamental factor in AD development (Sperling et al., 2020), mice allowed to progress into old age may better represent the clinical manifestations of human AD. Such old mice could offer greater insights into the potential translation of effective therapies.

Beyond the brain, a growing number of studies have provided evidence for AD-specific protein aggregation, vascular pathology, and markers of neuroinflammation in the neurosensory retina of various transgenic, induced, and spontaneous animal models of AD (Chang et al., 2020; Chiasseu et al., 2017; Do et al., 2019; Doustar et al., 2017; Grimaldi et al., 2018; Hampel et al., 2018; Hart et al., 2016; Koronyo et al., 2012; Lei et al., 2017), as well as in human AD patients (Alexandrov et al., 2011; den Haan et al., 2018; Hadoux

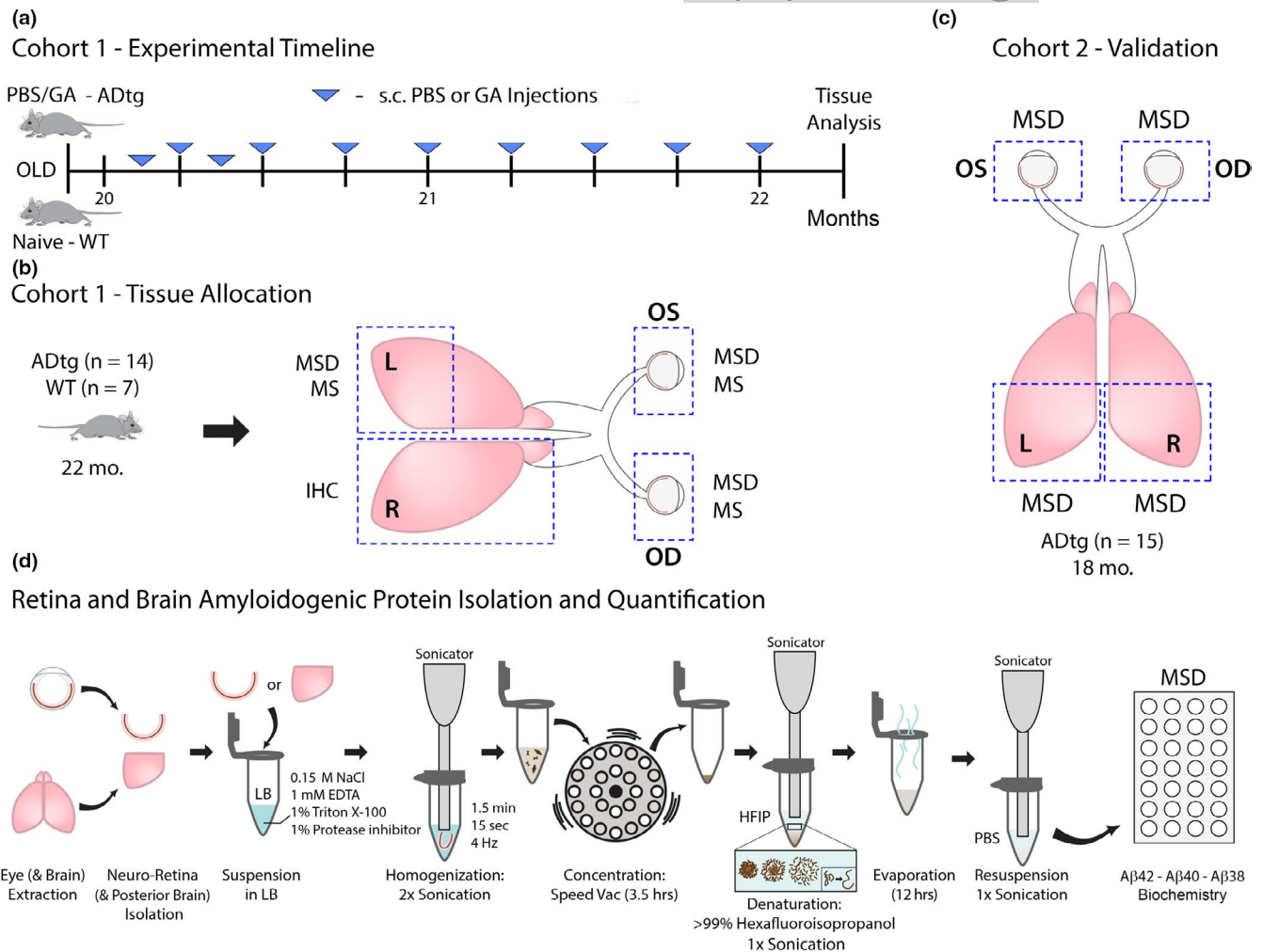


**FIGURE 1** Experimental design and intervention timeline assessing cerebral and retinal tissues in old, late-stage ADtg mice. (a) Experimental timeline for mouse Cohort 1: 20-month-old APP<sub>SWE</sub>/PS1<sub>ΔE9</sub> (ADtg) mice underwent weekly, subcutaneous injections of glatiramer acetate (GA, also known as Copaxone®; 100 μg) for a 2-month duration ( $n = 7$  mice). Age- and sex-matched ADtg mice were subcutaneously injected with PBS in the same regimen and naïve non-transgenic (WT) littermates were used as controls ( $n = 7$  mice per group). (b) One week following the last injection, mice were sacrificed, and tissues were collected as described. Paired brains and eyeballs from Cohort 1 were allocated for further analyses: the right (R) cerebral hemisphere was used for immunohistochemistry (IHC), the left (L) posterior brain was used for quantitative biochemical Meso Scale Discovery (MSD) and Mass Spectrometry (MS) assays, and both oculus sinister (OS, left) and oculus dexter (OD, right) eyeballs were collected, the neurosensory retinae isolated, and proteins assessed by MSD and MS analyses. OS and OD retinae were separately analyzed by MSD and pooled together for MS analysis. (c) Cohort 2 was comprised of old ADtg mice ( $n = 15$  mice; average age of 18 months). L and R posterior brains as well as OS and OD eyeballs were collected and analyzed separately for A $\beta$  proteins by MSD. (d) Preparation of mouse neuro-retina and posterior brain A $\beta$  proteins for quantification by MSD. Each tissue was prepared separately for analysis (OS retina, OD retina, and left and right posterior brains). The protocol involves suspension in lysis buffer (LB), homogenization via sonication, concentration with speed vac, and protein denaturation with hexafluoroisopropanol (HFIP) followed by evaporation and resuspension in PBS prior to protein concentration analysis

et al., 2019; Koronyo et al., 2017; Koronyo-Hamaoui et al., 2011; La Morgia et al., 2016; Schon et al., 2012; Schultz et al., 2020; Shi et al., 2020; Tsai et al., 2014). Biochemical analyses of A $\beta$ <sub>40</sub> and A $\beta$ <sub>42</sub> peptide levels in retinal and brain tissues from several transgenic murine models and AD patients revealed increases in both peptides in the AD retina as compared to controls, with higher levels in the brain and correlations with brain levels (La Morgia et al., 2016; Schultz et al., 2020; Shi et al., 2020). However, assessment of such relationships between paired retinas derived from oculus sinister (OS) versus oculus dexter (OD) eyes and left versus right cerebral hemispheres for

A $\beta$  load was not previously undertaken. This is especially true for response to therapy and in old ADtg mice. A recent study showed the accumulation of A $\beta$ <sub>40</sub> and A $\beta$ <sub>42</sub> peptides in whole ocular tissues of 5 $\times$  FAD transgenic mice with a reduction in ocular A $\beta$  following neprilysin treatment (Parthasarathy et al., 2015). Although these findings are significant, the inclusion of non-neuronal tissue and the lack of analyzed brain tissues hinder the ability to evaluate connections between the neuro-retina and brain. In this context, we previously demonstrated a comparable A $\beta$ -deposit reduction in retinal and cerebral tissues of 12-month-old ADtg mice subjected



to immunomodulation with MOG-45D (altered myelin-derived peptide) loaded on dendritic cells (Koronyo-Hamaoui et al., 2009, 2011) and subsequently showed the feasibility to noninvasively detect progressive appearance and clearance of individual retinal A $\beta$  plaques following GA immunization (Koronyo et al., 2012).

Collectively, these early studies provide the rationale to explore the relationship between retinal and cerebral pathology, including accumulation of both non-amyloidogenic and disease-associated amyloidogenic A $\beta$  alloforms, in old age and later stages of disease. There is also a need to study the responses to immunomodulation intervention in more clinically relevant, aged murine models and to quantitatively determine parallels between the brain and retina. Addressing the above unknowns, this study provides evidence for the predictability of cerebral A $\beta_{42}$  and A $\beta_{40}$  burden via quantitative measurements of OS and OD retinal counterparts in old ADtg mice. Moreover, in addition to identifying similar responses in the neuro-retina and the brain this study demonstrates the efficacy of GA immunomodulation in restricting vascular pathology and neuroinflammation while improving synaptic density at such late-stage disease.

## 2 | RESULTS

### 2.1 | Lateralization of A $\beta$ levels in retinae and brain hemispheres from old AD model mice

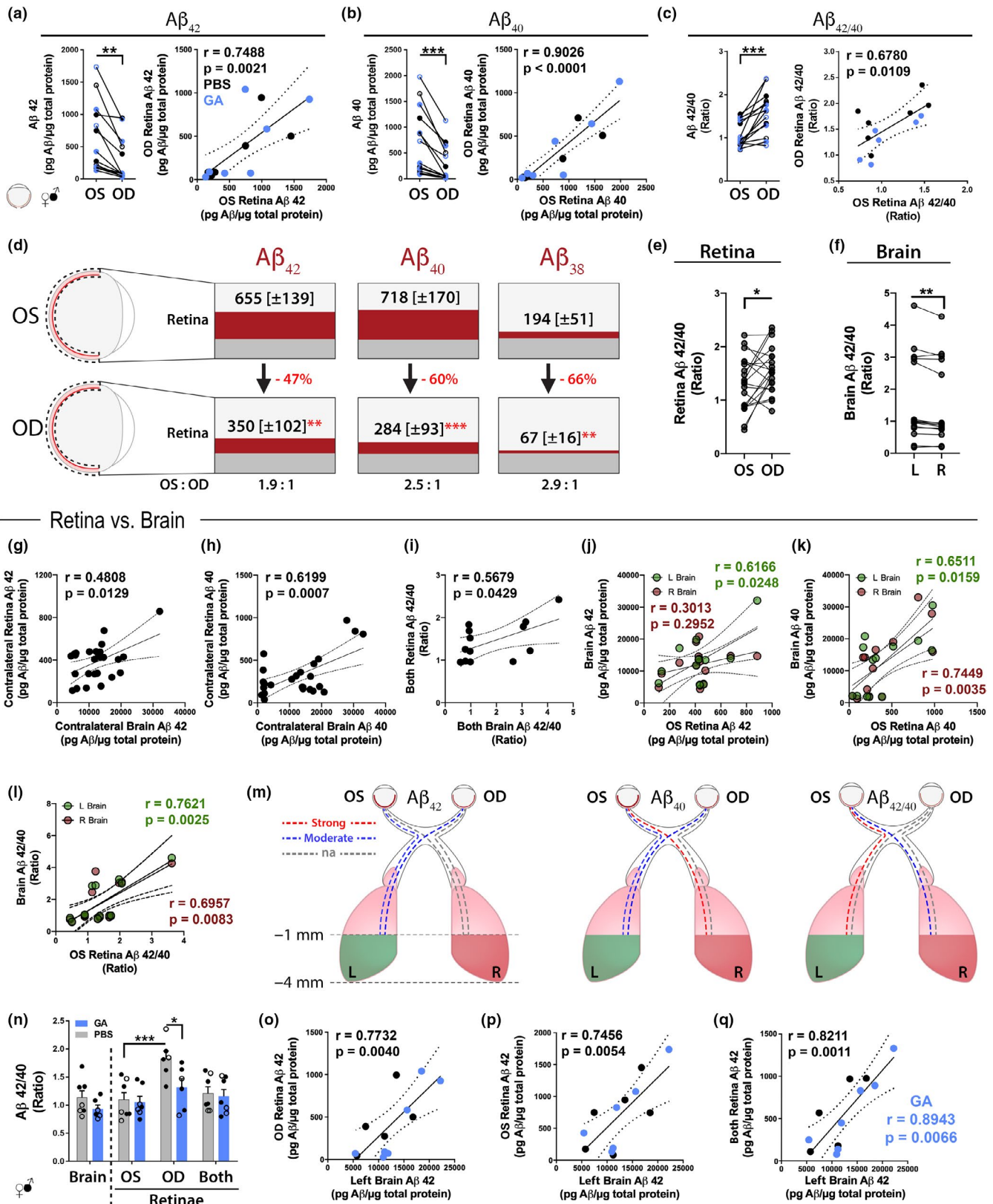
To investigate levels of disease-associated amyloidogenic (A $\beta_{1-42}$  and A $\beta_{1-40}$ ) and non-amyloidogenic (A $\beta_{1-38}$ ) alloforms in neurosensory retina and brain tissues, as well as evaluate the relationship between retinal and brain A $\beta$  burden, we analyzed two cohorts of 18- and 22-month-old, late-stage transgenic APP<sub>SWE</sub>/PS1 $_{\Delta E9}$  (ADtg) mice (Figure 1a–c). Further, to assess retinal and brain A $\beta$  pathology in response to immunotherapy in old mice, a cohort of

20-month-old ADtg mice underwent GA immunization and were compared against age- and sex-matched PBS-control ADtg and naive WT mice (Cohort 1, experimental timeline and GA immunization regimen are shown in Figure 1a;  $n = 7$  mice per group). Cohort 2 composed of old, untreated 18-month-old ADtg mice ( $n = 15$ ) were allotted to validate concentrations of A $\beta$  alloforms in retinal and brain tissues. Retinae derived from OS and OD eyes, as well as left and right posterior brains, were allocated for histological (immunohistochemistry–IHC) or biochemical (Meso Scale Discovery–MSD, mass spectrometry–MS) analyses as outlined in Figure 1b–c. To this end, we established a new protocol encompassing extraction, enrichment, and hexafluoroisopropanol (HFIP)-mediated unfolding of A $\beta$  proteins (Figure 1d).

Levels of A $\beta_{42}$ , A $\beta_{40}$ , and A $\beta_{38}$  alloforms measured by MSD in paired OS and OD retinae of PBS-control and GA-immunized ADtg mice (Cohort 1) are displayed in Figure 2a–b (extended data in Figure S1A–C). Another principle characteristic of AD neuropathology is the ratio between A $\beta_{42}$  and A $\beta_{40}$ . We further calculated and compared A $\beta_{42/40}$  ratios between OS and OD retinae in this cohort (Figure 2c). Consistent disparities in A $\beta$  alloform accumulation between paired OS and OD retinae were found, with significantly higher levels in the OS versus the OD retina in old transgenic mice (A $\beta_{42}$ ,  $p = 0.0015$ ; A $\beta_{40}$ ,  $p = 0.0005$ ; and A $\beta_{38}$ ,  $p = 0.0063$ , by paired two-tailed Student's  $t$  test; Figures 2a–b and S1A). Lateralization of A $\beta$  alloforms was independent of treatment group and gender (females: A $\beta_{42}$ ,  $p = 0.0346$ ; A $\beta_{40}$ ,  $p = 0.0209$ ; A $\beta_{38}$ ,  $p = 0.0280$ ; males: A $\beta_{42}$ ,  $p = 0.0056$ ; A $\beta_{40}$ ,  $p = 0.0122$ ; A $\beta_{38}$ ,  $p = 0.2036$ ; by paired two-tailed Student's  $t$  test). Interestingly, paired analysis of A $\beta_{42/40}$  ratio similarly showed lateralization, albeit higher in OD versus OS retina ( $p = 0.0004$ , paired two-tailed Student's  $t$  test; Figure 1c). Despite this asymmetry, tight correlations in levels of A $\beta$  alloforms and A $\beta_{42/40}$  ratios were revealed between paired OS and OD retinae (Pearson's correlation coefficient  $r = 0.75$  and  $p = 0.0021$  for A $\beta_{42}$ ,  $r = 0.90$  and  $p < 0.0001$  for A $\beta_{40}$ ,  $r = 0.94$  and  $p < 0.0001$  for A $\beta_{38}$ ,

**FIGURE 2** Retinal and cerebral A $\beta$  alloforms in old ADtg mice and following immunotherapy. (a–c) Analysis of A $\beta_{1-42}$ , A $\beta_{1-40}$ , and A $\beta_{42/40}$  ratio levels ( $n = 7$  mice per group) in OS versus OD retinae from Cohort 1 of GA-immunized (blue) and PBS-control (black) old ADtg mice. Data indicate A $\beta$  concentrations for individual mouse in OS versus OD retina analyzed by paired Student's  $t$  test. Pearson's  $r$  correlations between levels of each A $\beta_{1-42}$ , A $\beta_{1-40}$ , and A $\beta_{42/40}$  ratio in OS and OD retinae are also shown ( $n = 13$ – $14$  mice; right graphs). (d) Schematic display of A $\beta_{1-42}$ , A $\beta_{1-40}$ , and A $\beta_{1-38}$  alloform concentrations (Average;  $\pm$  SEM in brackets) in each retina from Cohort 1. Data presented in pg A $\beta$  per  $\mu$ g total protein. Lower percentages of amyloid levels in OD versus OS retinae are shown in red, and OS to OD ratios of A $\beta$  concentrations are indicated below. (e–f) A $\beta_{42/40}$  ratios as assessed by MSD analysis in paired OS versus OD retinae from ADtg mice (e; Cohorts 1 and 2 without GA group;  $n = 20$  mice) and in paired L versus R brains from Cohort 2 ADtg mice (f;  $n = 15$  mice). Lateralization was determined by paired Student's  $t$  test. (g–m) Pearson's  $r$  correlations between retinal and cerebral A $\beta$  burden in ADtg mice from Cohort 2. (g–h) Contralateral correlations between OS retina versus R brain and OD retina versus L brain for (g) A $\beta_{42}$  and (h) A $\beta_{40}$  levels ( $n = 12$ – $14$ ). (i) Correlation between average retinal and average cerebral A $\beta_{42/40}$  ratios. (j–l) Unilateral correlations of OS retina versus L brain (green) or versus R brain (red) for (j) A $\beta_{42}$ , (k) A $\beta_{40}$ , and (l) A $\beta_{42/40}$  ratio ( $n = 13$ ). (m) Schematic illustration portraying strength of associations between each retina and each posterior brain for A $\beta_{42}$ , A $\beta_{40}$ , and A $\beta_{42/40}$  ratio in old ADtg mice. The analyzed posterior brain includes tissue between  $-1$  and  $-4$  mm bregma. Strong associations in red ( $r > 0.7$ ), moderate associations in blue ( $r = 0.5$ – $0.7$ ), and weak or no associations (na) in gray ( $r = 0.0$ – $0.5$ ). (n–q) Analysis of retinal versus cerebral A $\beta$  levels in Cohort 1 old ADtg mice following GA immunization. (n) Brain and retinal A $\beta_{42/40}$  ratios in PBS-control versus GA-immunized ADtg mice ( $n = 7$  mice per group). (o–q) Pearson's  $r$  correlations between levels of A $\beta_{42}$  in L brain and (o) OD retina, (p) OS retina, and (q) an average of both retinae ( $n = 14$  mice). Strong correlations in A $\beta_{1-42}$  burden between brain and retinal tissues are especially apparent following GA immunization (q). Graphs display individual data point for each mouse, with bar graphs also indicating group mean and standard error of mean (SEM) values. Mouse sex is designated as filled circles for males and open circles for females (gender not shown in correlation graphs). \* $p < 0.05$ , \*\* $p < 0.01$ , \*\*\* $p < 0.001$  assessed by paired Student's  $t$  test for two-group comparisons, and a two-way ANOVA with Sidak's post-test for group analysis for brain and retinal tissues

## Lateralization



$r = 0.68$  and  $p = 0.0109$  for  $A\beta_{42/40}$ ; Figures 2a-c and S1A). Figure 2d illustrates the average ( $\pm$ SEM)  $A\beta$  burden in OS versus OD retinae ( $655 \pm 139$  vs.  $350 \pm 102$  for  $A\beta_{42}$ ;  $718 \pm 170$  vs.  $284 \pm 93$  for  $A\beta_{40}$ ;

$194 \pm 51$  vs.  $67 \pm 16$  for  $A\beta_{38}$ , respectively; pg  $A\beta$  per  $\mu$ g total protein).  $A\beta$  levels are 47%–66% lower in the OD retina as compared to their corresponding levels in the OS retina in this old mouse model



(Figure 2d). Additional data on retinal A $\beta$  pathology from Cohort 1 are included in Figure S1B–F.

In light of the significant disparities in A $\beta$  levels between OS versus OD retina, we aged an additional mouse Cohort 2 (18-month-old ADtg mice) and assessed lateralization of A $\beta$  burden in paired retinae and brains at advanced disease stage without intervention (Figure 2e–f; extended data in Figure S1G–L). MSD results from combined Cohorts 1 and 2 validated a significant OS retina dominant lateralization for A $\beta_{42}$  and A $\beta_{40}$  levels ( $p = 0.0057$  and  $p = 0.0082$ , respectively, by two-tailed paired Student's  $t$  test;  $n = 21$ , Figure S1G–H). Retinal A $\beta_{38}$  alloforms were below detectable levels for most retinae from this cohort. As it refers to disease-relevant A $\beta_{42/40}$  ratios, OD retina dominant lateralization was identified in these old ADtg mice ( $p = 0.0335$ , by two-tailed paired Student's  $t$  test; Figure 2e). In agreement with the above results, positive correlations were found between levels of A $\beta_{42}$ , A $\beta_{40}$ , and A $\beta_{42/40}$  in OS versus OD retinae (Figure S1G–I). Correlations between OS and OD retinae for A $\beta_{42}$  levels were consistently strong (Figure S1G; Pearson's  $r = 0.7123$  and  $p = 0.0003$ ).

These findings in OS versus OD retinae led to the question of whether lateralization in A $\beta$  levels also exists in the brains of old ADtg mice. Examination of bilateral brain tissues from Cohort 2 for A $\beta$  alloforms by MSD analysis revealed left posterior brain-dominant lateralization in A $\beta_{42/40}$  ratios ( $p = 0.0061$ , paired two-tailed Student's  $t$  test;  $n = 15$ ; Figure 2f, extended data in Figure S1J–L). Although no one-side (left or right) dominance of posterior brain lateralization was found for individual A $\beta_{42}$ , A $\beta_{40}$ , and A $\beta_{38}$  alloforms, consistent disparities in their levels were obtained between the two hemispheres (Figure S1J–K; data not shown for A $\beta_{38}$ ). Similar to the retina, all A $\beta$  alloform levels significantly correlated between left and right posterior brains (Pearson's  $r = 0.59$  and  $p = 0.0279$  for A $\beta_{42}$ ;  $r = 0.76$  and  $p = 0.0009$  for A $\beta_{40}$ ;  $r = 0.68$  and  $p < 0.0100$  for A $\beta_{38}$ ; Figure S1J–K). An especially strong correlation was found for levels of A $\beta_{42/40}$  ratio ( $r = 0.98$  and  $p < 0.0001$ ; Figure S1L). Moreover, levels of each amyloidogenic A $\beta_{42}$  and A $\beta_{40}$  alloform strongly predicted co-accumulation in the same retina or brain location (Pearson's  $r > 0.90$  and  $p < 0.0001$  across all retinal and brain tissues; Figure S2A–F).

## 2.2 | Association between retinal and brain A $\beta$ levels

Next, to determine the feasibility of predicting cerebral A $\beta$  burden via its levels in the retina, brain levels were correlated against contralateral or ipsilateral, each OS and OD, and both retinae in old ADtg mice without intervention (Figures 2g–m and S2G–R and S3A–L; Cohort 2). This assessment revealed that at advanced disease stage, significant correlations exist between levels in contralateral retina and brain tissues (OS retina to right brain or OD retina to left brain) for both amyloidogenic alloforms (Pearson's  $r = 0.48$  and  $p = 0.0129$  for A $\beta_{42}$ ,  $r = 0.62$  and  $p = 0.0007$  for A $\beta_{40}$ ;  $n = 26$ ; Figure 2g–h; extended data on ipsilateral and contralateral correlations for each A $\beta$  alloform and A $\beta_{42/40}$  ratios in Figure S2G–J). Cumulative peptide values for both retina and both brains from each

mouse were compared, indicating significant correlations of retinal to brain A $\beta_{42/40}$  ratios and A $\beta_{40}$  levels (Pearson's  $r = 0.57$ ,  $p = 0.0429$  and  $r = 0.59$ ,  $p = 0.0328$ , respectively;  $n = 13$ ; Figures 2i and S2L), and a significant correlation of OS retinal A $\beta_{42}$  against both brain A $\beta_{42}$  levels ( $r = 0.595$  and  $p = 0.0321$ ; Figure S2M). Individual correlations between OS or OD retina compared to paired left or right brain for each A $\beta$  alloform demonstrated the greatest degree of associations between OS retina to left brain for A $\beta_{42}$  (Pearson's  $r = 0.62$  and  $p = 0.0248$ ; Figure 2j) and OS retina to left and right brains for A $\beta_{40}$  ( $r = 0.65$  and  $p = 0.0159$  for left and  $r = 0.74$  and  $p = 0.0035$  for right brain; Figure 2k). Similarly, most significant correlations for A $\beta_{42/40}$  ratios were identified for OS retina to left and right brains ( $r = 0.76$  and  $p = 0.0025$  for left and  $r = 0.696$  and  $p = 0.0083$  for right brain;  $n = 13$ ; Figure 2l). Figure 2m illustrates all individual Pearson's ( $r$ ) correlations, with blue and red dashed lines designating moderate to strong significant associations (extended data in Figure S3A–L).

## 2.3 | Retinal and cerebral A $\beta$ levels strongly correlate in response to intervention

To evaluate effects of GA immunization on levels of retinal and brain A $\beta$  alloforms in old ADtg mice (Cohort 1), we initially compared MSD data between GA-immunized and PBS-control groups (Figures 2n and S1D–F). Both the retinae and the posterior left brain did not show significant reductions in A $\beta$  levels following GA immunization at this advanced, late-stage disease (Figure S1D–F). However, A $\beta_{42/40}$  ratio levels in the OD retina were significantly reduced in GA-immunized as compared to PBS-control mice ( $p = 0.0246$ , two-way ANOVA with Sidak's post-test; Figure 2n). Despite marked differences between brain and retina levels for each A $\beta$  alloform (Figure S1D–F), very similar A $\beta_{42/40}$  ratios were detected across the two CNS tissues, with the exception of higher ratio in the OD retina in PBS-control ADtg mice ( $p = 0.0007$ ; by two-way ANOVA and Sidak's post-test; Figure 2n).

To determine possible connections between retino-cerebral A $\beta$  levels in response to GA immunization, levels of A $\beta_{42}$ , A $\beta_{40}$ , and A $\beta_{38}$  alloforms in the left posterior brain were correlated against OD, OS, or both retinae in GA-immunized and control mice (Figures 2o–q and S3M–R; Cohort 1). Strong linear correlations were identified between cerebral and OD, OS, and both retinal A $\beta_{42}$  levels ( $r = 0.77$  and  $p = 0.004$ ,  $r = 0.746$  and  $p = 0.0054$ ,  $r = 0.82$  and  $p = 0.0011$ , respectively;  $n = 13$ ; Figure 2o–q). These results are in accordance with retinal A $\beta_{42}$  levels' correlation with the left posterior brain, as described for untreated old ADtg mice above (Cohort 2; Figure 2j). Importantly, a separate Pearson's  $r$  analysis for GA-immunized ADtg mice revealed an even stronger association between retinal and cerebral A $\beta_{42}$  loads ( $r = 0.89$  and  $p = 0.0066$ ; Figure 2q, in blue). Retinal and brain correlations for A $\beta_{40}$  or non-amyloidogenic A $\beta_{38}$  levels were weaker, reaching statistical significance between OD/OS retina to left posterior brain for A $\beta_{40}$  and A $\beta_{38}$  ( $r = 0.58$  and  $p = 0.0391$  and  $r = 0.58$  and  $p = 0.0499$ , respectively; Figure S3M–R).



## 2.4 | Immunomodulation ameliorates vascular and parenchymal A $\beta$ deposits in old ADtg mice

To further explore the therapeutic potential of immunomodulation in old, advanced disease stage mice, we performed in-depth histological analyses on brain tissues from Cohort 1. As outlined in Figure 1b, both retinas and left posterior brain tissues were allocated for biochemical MSD and MS analyses, and additionally, the right brain hemispheres were evaluated by IHC analyses. Histological examination of various AD-relevant biomarkers, including A $\beta$ -plaque burden, both vascular and parenchymal deposits, ionized calcium-binding adaptor molecule 1 (Iba-1), protein tyrosine phosphatase receptor type C (CD45), glial fibrillary acidic protein (GFAP), and glutamine synthetase (GS), was conducted on brain tissues encompassing the following regions as specified in Figure 3a: hippocampus (Hipp), cingulate cortex/retrosplenial area (Ctx), and entorhinal cortex/piriform area (Ent; Figures 3 and 4; extended data in Figures S4–S8). Representative microscopic images of cortical regions in GA-immunized versus PBS-control old ADtg mice revealed lower frequency of large 6E10<sup>+</sup>-A $\beta$  plaques and surrounding GFAP<sup>+</sup> astrogliosis in the GA-immunized group (Figure 3b vs. 3c). Stereological analysis of A $\beta$ -plaque area verified significant reductions in all analyzed brain regions following GA immunization (Hipp: 40% reduction,  $p = 0.0003$ ; Ctx: 48% reduction,  $p < 0.0001$ ; Ent: 45% reduction,  $p < 0.0001$ ; Total brain: 45% reduction,  $p < 0.0001$ ; by one-way ANOVA and Sidak's post-test; Figure 3d). Further, we analyzed vascular 6E10<sup>+</sup> A $\beta$  deposits in the Ent of GA-immunized versus PBS-control old ADtg mice (Figure 3e–f). Vascular A $\beta$  pathology was categorized along a scale of cerebral amyloid angiopathy (CAA; from none = 0 to severe = 4 scores; Figure 3f). Our quantitative evaluation suggests a significant 63% reduction in vascular amyloidosis scores following GA immunization ( $p = 0.0093$ , by unpaired two-tailed Student's *t* test; Figure 3e).

To explore A $\beta$  plaque subtypes possibly targeted by GA immunization, we developed a semi-manual method to measure individual plaque morphology, classified by size, shape, and density, as presented in Figure 3g–h. Our analysis included 6E10<sup>+</sup>-A $\beta$  perimeter area, length (maximum diameter), and width (minimum diameter) of individual plaques in GA-immunized versus PBS-control mice, further identifying plaque subtypes as dense-core (DC) or non-DC (Figure 3g–h). Assessment of individual A $\beta$ -plaque area within the Ent showed a reduction in plaque size of over 20% ( $p = 0.0167$ , by unpaired two-tailed *t* test; Figure S4A). Structural classification of A $\beta$  plaques by density revealed a substantial decrease in number and area of DC plaques, along with other size measurements of this plaque subtype (Figure 3i–k; extended data in Figure S4B–C). GA immunization in these old ADtg mice resulted in a consistently smaller average area, lower quantity, and shortened length of the dense-core plaques ( $p = 0.0054$  with 28% reduction in size,  $p = 0.0010$  with 47% reduction in count, and  $p < 0.0029$  with 16% reduction in length of DC plaques; Figure 3i–k). These differences did not reach statistical significance for non-DC diffuse plaques (Figure S4D–F).

Further stratification by plaque size revealed that GA immunization especially modified large plaques ( $p = 0.0331$  with 24% reduction in area,  $p = 0.0055$  with 25% decrease in width, and  $p = 0.0017$  with 28% decrease in length of large plaques; Figure 3l–n; extended data on other plaque types and measurements see Figure S4G–I). Overall, these results may uncover critically beneficial effects of immunomodulation on limiting pre-existing A $\beta$  deposits at an old age and advanced disease stage.

## 2.5 | Immunomodulation curbs microgliosis and astrogliosis with increased recruitment of peripheral myelomonocytes

Neuroinflammatory responses mediated by innate immune cells surrounding A $\beta$  plaques have been implicated in modulating plaque structure and subsequent toxicity in both animal models of AD and human patients (Rasmussen et al., 2017; Vilella et al., 2018; Wang et al., 2016). Of these, microgliosis and reactive astrocytes are established features around A $\beta$  plaque lesion sites (Heneka et al., 2015; Osborn et al., 2016; Rajendran & Paolicelli, 2018; Rodriguez-Arellano et al., 2016; Wyss-Coray & Mucke, 2002). Further, the involvement of peripheral immune cells has been shown in both pathological processes (Bradshaw et al., 2013; Ferretti et al., 2016; Gate et al., 2020; Jevtic et al., 2017; Li et al., 2020; Pluvinage & Wyss-Coray, 2020) and protective clearance of cerebral A $\beta$ , reduction of neuroinflammation, and promotion of tissue regeneration (Bernstein, et al., 2014; Butovsky et al., 2007; Koronyo et al., 2015; Koronyo-Hamaoui et al., 2009, 2020; Lebson et al., 2010; Li et al., 2020; Rentsendorj et al., 2018; Simard et al., 2006). To assess changes in microgliosis and infiltrating myeloid cell populations, serial brain sections were immunolabeled against Iba1, marker of brain-resident microglia and peripheral myeloid cells, CD45<sup>hi</sup> for infiltrating hematopoietic immune cells, and GFAP for astrocytes.

There were substantial increases in cerebral Iba1<sup>+</sup> microgliosis, with activated-type cell morphology surrounding plaques, as well as in Iba1<sup>+</sup>CD45<sup>hi</sup> myeloid cell population in old PBS-injected ADtg mice when compared to matched naïve WT mice (Figure 4a–b; extended representative images in Figure S5–S7). This was evident throughout the analyzed brain regions, including Hipp, Ctx, Ent, and total brain regions ( $p < 0.0001$  for all comparisons, by one-way ANOVA and Sidak's post-test; Figure 4a–b). Importantly, even at old age, our immunomodulation strategy considerably diminished Iba1<sup>+</sup> microgliosis in ADtg mice, with an average reduction of 56% in total brain regions ( $p < 0.0001$ , by one-way ANOVA and Sidak's post-test; Figure 4a). In contrast, immunization further induced recruitment of peripherally derived Iba1<sup>+</sup>CD45<sup>hi</sup> myeloid cells into the Hipp, Ctx, and Ent regions, by an average 78% increase in total brain in GA-immunized vs PBS-control ADtg mice ( $p < 0.001$ – $0.0001$ ; Figure 4b). Colocalization analysis of Iba1<sup>hi</sup>CD45<sup>hi</sup> out of total Iba1<sup>+</sup> population revealed that the portion of infiltrating innate immune cells was significantly increased from 27% in PBS-control mice to 40% in GA-immunized old ADtg mice ( $p = 0.0061$ , unpaired Student's *t* test; Figure 4c).



Representative microscopic images of PBS-control and GA-immunized old ADtg mouse brains show GFAP<sup>+</sup> reactive astrocyte and Iba1<sup>+</sup> myelomonocytic cell populations surrounding 4G8<sup>+</sup>-A $\beta$  plaques (Figure 4d-f). Observations of inflammatory Iba1<sup>+</sup> cells found higher numbers per plaque site in GA-treated as compared to PBS-control brains and displayed a higher colocalization with A $\beta$  (Figure 4d-f), which may indicate increased A $\beta$ -plaque uptake. Representative microscopic images in Figure 4g demonstrate the

abundance of cortical Iba1<sup>+</sup>CD45<sup>hi</sup> tagged peripheral immune cells following GA immunomodulation compared to PBS treatment (extended images in Figures S5-S7). Quantification of the ratio between Iba1<sup>+</sup>CD45<sup>hi</sup> area and 6E10<sup>+</sup> A $\beta$ -plaque area revealed a substantial ~3-fold increase in these infiltrating myelomonocytes per plaque site in the GA-immunized versus PBS-control mouse brains ( $p < 0.0001$ , by unpaired Student's  $t$  test; Figure 4h).

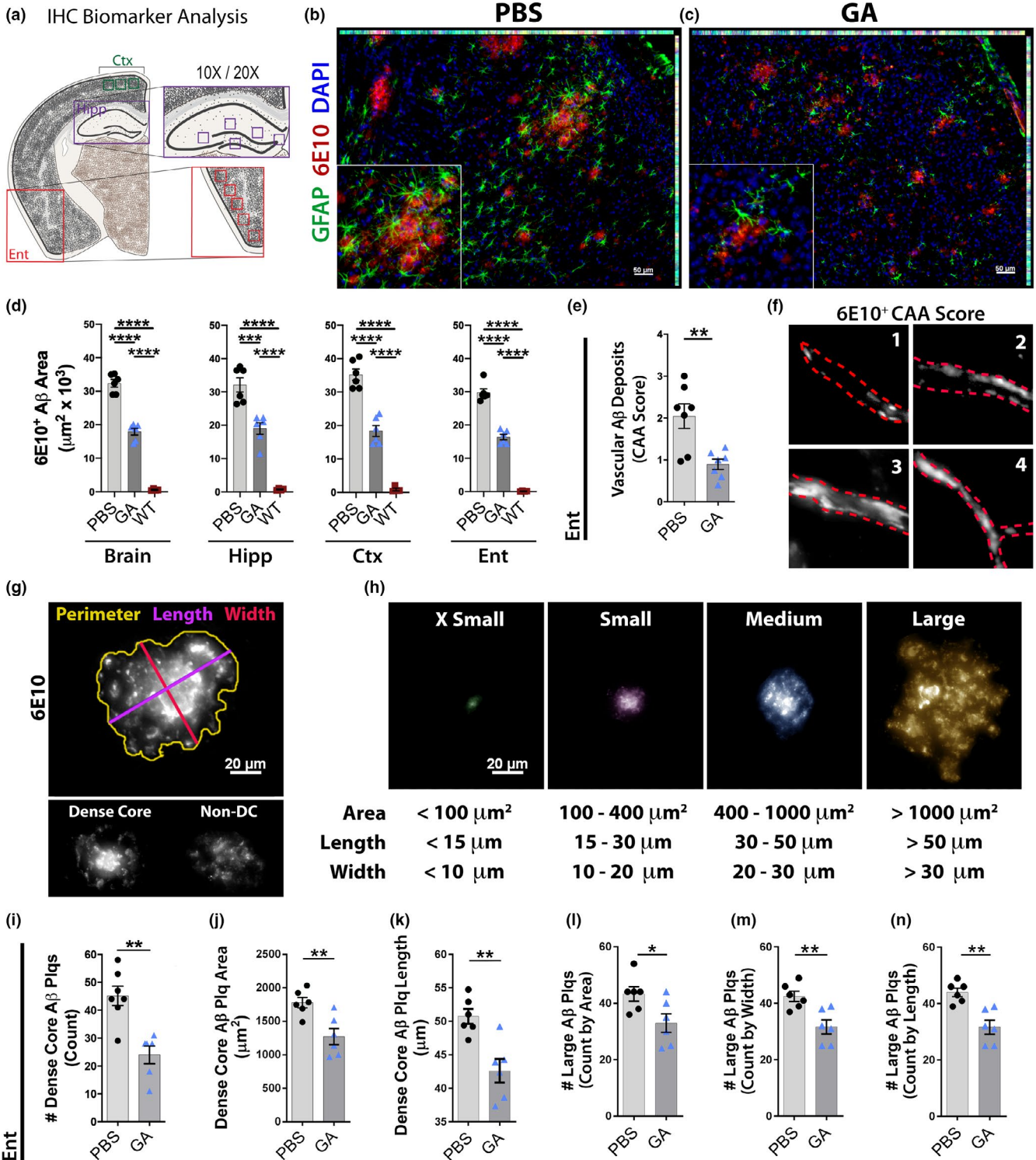






**FIGURE 3** Decreased cerebral A $\beta$ -plaque pathology and vascular amyloidosis in old ADtg mice following GA immunotherapy. (a) Cerebral map indicating specific brain regions analyzed by IHC; regions include the cingulate cortex/retrosplenial area (Ctx), hippocampus (Hipp), and entorhinal cortex/piriform area (Ent). (b–c) Representative coronal sections of a cortical region stained for astrocytes (GFAP, green), A $\beta$  plaques (6E10, red), and cell nuclei (DAPI; blue) in (b) PBS-control and (c) GA-treated ADtg mice. (d) Quantitative IHC analysis of 6E10<sup>+</sup> A $\beta$ -plaque area in total brain, Hipp, Ctx, and Ent of all experimental groups ( $n = 6$  mice per group). (e) Analysis of cerebral amyloid angiopathy (CAA) scores in the Ent of GA-immunized versus untreated (PBS) old ADtg mice ( $n = 7$  mice per group). (f) Representative images illustrating the scoring method used to assess vascular 6E10<sup>+</sup> A $\beta$  deposits [termed as cerebral amyloid angiopathy (CAA) scores], with scale ranges from 0 to 4, with higher scores for greater vascular A $\beta$  pathology. (g) Representative images and measurements of perimeter, length (largest diameter), and width (smallest diameter) acquired per A $\beta$  plaque (top); Dense-core and non-dense-core/diffuse plaque subtypes are demonstrated (bottom). (h) Microscopic images showing classification of plaque by size, as defined by area, length and width. Accordingly, plaques were categorized into four subgroups: x-small, small, medium, and large. (i–k) Quantitative analysis of dense-core plaque phenotype within the Ent of GA-immunized versus PBS-control ADtg mice, including (i) total count, (j) average area, and (k) length. (l–n) Quantitative analysis of large A $\beta$ -plaque count, as determined by (l) area, (m) width, and (n) length, within the Ent of GA-immunized versus PBS-control ADtg mice ( $n = 6$ –7 mice per group). Bar graphs indicate mean, standard error of mean (SEM), and individual data points. \* $p < 0.05$ , \*\* $p < 0.01$ , \*\*\* $p < 0.001$ , \*\*\*\* $p < 0.0001$  assessed by unpaired Student's  $t$  test for two-group comparisons, and a one-way ANOVA with Tukey's post-test for three or more groups

Correlational analysis revealed a very tight inverse association between CD45<sup>hi</sup> area and 6E10<sup>+</sup>-plaque area in Ctx of old ADtg mice ( $r = -0.96$  and  $p < 0.0001$ ; Figure 4i; extended Pearson's correlations between either brain-resident or peripherally derived myeloid cells and plaque area in different AD-relevant brain regions are in Figure S8A–B). When analyses were separated by experimental group, GA-treated mice retained a strong correlation between these infiltrating myeloid cells and plaque area, while the PBS-control group did not display a significant association ( $r = -0.97$  and  $p = 0.0016$ ,  $r = -0.54$  and  $p = 0.2669$ , respectively; Figure 4j). These results may indicate that cerebral infiltration of Iba1<sup>+</sup>CD45<sup>hi</sup> myeloid cells induced by GA immunization is strongly linked with clearance of A $\beta$  pathology.

GFAP is one of the key biomarkers for detecting reactive, scar-tissue related astrocytes (De Strooper & Karran, 2016; Osborn et al., 2016). Quantitative IHC analysis of GFAP<sup>+</sup> reactive astrocyte area showed greater cerebral astrogliosis in PBS-control old ADtg mice as compared to the old wild-type mice ( $p < 0.0001$ ; Figure 4k). GA immunization consistently curtailed astrogliosis by 30 and 35% in various brain regions, including Hipp, Ctx, Ent, and total brain ( $p < 0.0001$ ,  $p < 0.0001$ ,  $p = 0.0361$ , and  $p < 0.0001$ , respectively, by one-way ANOVA and Tukey's post-test correction; Figure 4k). Moreover, levels of cerebral GFAP<sup>+</sup> astrogliosis directly correlated with 6E10<sup>+</sup>-A $\beta$  burden (Pearson's  $r = 0.84$  and  $p = 0.0006$ ; Figure 4l; extended correlation analyses per brain region in Figure S8C).

Next, we evaluated the astrocyte-specific biomarker glutamine synthetase (GS), an enzyme associated with GFAP reactivity and responsible for synaptic recycling of extracellular glutamate (Rudy et al., 2015; Son et al., 2019; Zou et al., 2011). Peroxidase-based immunostaining for GS in coronal brain sections demonstrated morphological and intensity differences between GA-immunized and PBS-control old ADtg mice (Figure S8D). The GA-immunized group showed patterns indistinguishable from those of the non-transgenic WT mice. Across the three experimental groups, GFAP<sup>+</sup> reactive astrocyte area was associated with levels of GS immunoreactive area (Pearson's  $r = 0.72$  and  $p = 0.0005$ ; Figure S8E). Quantitative IHC analysis revealed a significant increase in

GS<sup>+</sup> area in PBS-control ADtg mice when compared to naïve WT mice ( $p = 0.0244$ ), with levels of GS normalized to WT in the Ent of GA-immunized ADtg mice ( $p < 0.05$ ; Figure S8F). Overall, our data suggest that GA immunization in old AD model mice has multiple beneficial effects toward reducing A $\beta$  plaques and restoring homeostatic microglia and astrocytic milieu, along with recruitment of Iba1<sup>+</sup>CD45<sup>hi</sup> myeloid cells.

## 2.6 | Synaptic preservation by GA immunization in old ADtg mice

The critical role of astrocytes in synaptic homeostasis, notably GS activity in regulating extracellular glutamate, prompted us to evaluate synaptic integrity and its relationship to astrocytic GS expression in these old ADtg mice. Histological examination of synaptic density was assessed for the post-synaptic density protein 95 (PSD95) biomarker in three AD-relevant brain regions, including hippocampal subregions, as outlined in Figure 5a. A significant increase in PSD95<sup>+</sup> area, reflecting improved synaptic density, was seen in the Ent region following GA immunization in ADtg mice, reaching equivalent levels to those measured in old WT littermates ( $p = 0.0411$  and 98% increase; Figure 5b; extended analysis of various anatomical hippocampal layers is shown in Figure S9A). Post-synaptic area was inversely correlated with astrocytic GS expression per cell, which was independent of treatment or genotype group ( $r = -0.57$  and  $p = 0.0127$ ; Figure 5c). Combined correlations of brain biomarkers indicate a significant inverse relationship between A $\beta$  pathology and post-synaptic area (PSD95) and direct associations of A $\beta$  burden with GFAP<sup>+</sup> reactive astrogliosis and astrocytic GS<sup>+</sup> area/cell ( $r = -0.75$  and  $p = 0.0014$ ,  $r = 0.95$  and  $p < 0.0001$ ,  $r = 0.73$  and  $p = 0.0019$ , respectively; Figure 5d). Representative fluorescent micrographs illustrate a substantial increase in PSD95<sup>+</sup> puncta number along with reduced astrogliosis and homeostatic astrocyte morphology following GA immunomodulation (Figure 5e–f; extended data in Figure S9B–C).

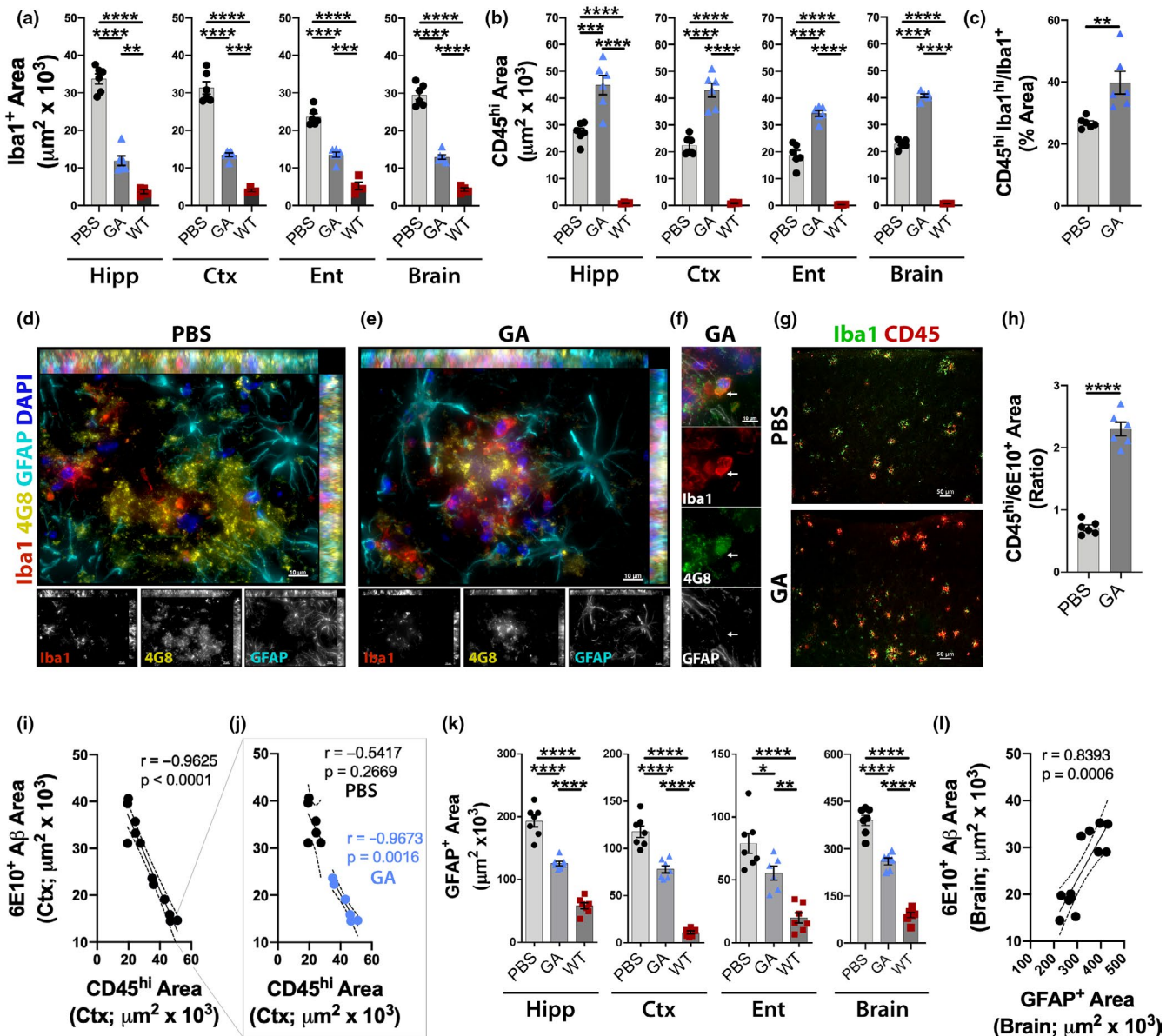


**FIGURE 4** Reduced cerebral microgliosis and astrogliosis along with peripheral monocyte recruitment following immunomodulation. (a) Quantitative IHC analysis of Iba1<sup>+</sup> microgliosis within predetermined brain regions: Hipp, Ctx, and Ent, as well as their average (Brain) in GA-immunized versus PBS-control ADtg mice, and in naïve WT mouse littermates. (b) Quantitative IHC analysis of Iba1<sup>+</sup>CD45<sup>hi</sup> infiltrating peripheral immune cells in brain regions and their average (Brain) ( $n = 6$  mice per group). (c) Analysis of percent area of Iba1<sup>hi</sup>/CD45<sup>hi</sup> peripheral monocytes population of Iba1<sup>+</sup> myeloid cell area within PBS-control and GA-immunized groups ( $n = 6$  mice per group). (d-e) Representative micrographs of inflammatory cells, GFAP<sup>+</sup> astrocytes (cyan) and Iba1<sup>+</sup> myelomonocytes (red), surrounding 4G8<sup>+</sup> A $\beta$  plaques (yellow) in the Ent cortex of old, late-stage (d) PBS-control and (e) GA-immunized ADtg mice. (f) A representative high-magnification micrograph of Ent cortex of GA-immunized ADtg mice with an Iba1<sup>+</sup> myelomonocytic cell (red) seen engulfing 4G8<sup>+</sup> A $\beta$ ; white arrow tags location between channels. (g) Representative micrographs of Iba1<sup>+</sup> myelomonocytes and CD45<sup>+</sup> hematopoietic immune cells within PBS-control and GA-immunized mice. (h) IHC analysis of CD45<sup>hi</sup> area/6E10<sup>+</sup> area ratio ( $n = 6$  mice/group). (i) Pearson's  $r$  correlation analysis between CD45<sup>hi</sup> hematopoietic cells and 6E10<sup>+</sup> A $\beta$ -plaque deposits in Ctx sections including PBS-control and GA-immunized mice ( $n = 12$  mice). (j) Separate Pearson's  $r$  correlations between CD45<sup>hi</sup> hematopoietic cells and 6E10<sup>+</sup> A $\beta$ -plaque deposits in old PBS-control and GA-immunized ADtg mice demonstrating retention of correlation with treatment. (k) Quantitative IHC analysis of GFAP<sup>+</sup> astrogliosis in total brain regions for all experimental groups ( $n = 6-7$  mice per group). (l) Pearson's  $r$  correlation analyses between GFAP<sup>+</sup> astrogliosis and 6E10<sup>+</sup> A $\beta$  for total brain plaque area in PBS-control and GA-immunized ADtg mice ( $n = 12$  mice). Bar graphs indicate mean, standard error of mean (SEM), and individual data points. \* $p < 0.05$ , \*\* $p < 0.01$ , \*\*\* $p < 0.001$ , \*\*\*\* $p < 0.0001$  assessed by unpaired Student's  $t$  test for two-group comparisons, and a one-way ANOVA with Tukey's post-test for three or more groups

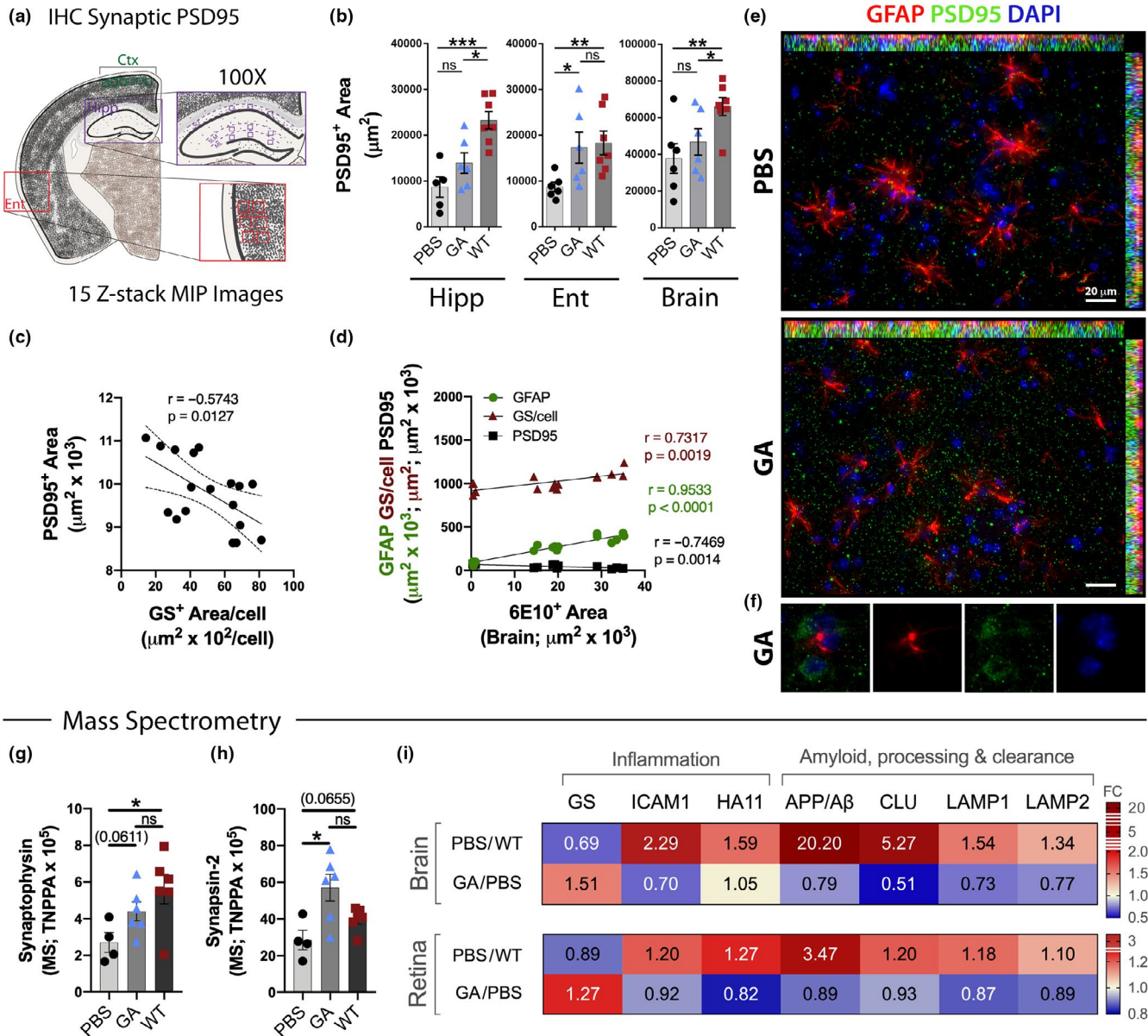


**FIGURE 5** Effects of GA immunization on synaptic density and AD-related retino-cerebral proteins in old ADtg mice. (a) Coronal section map displaying specific brain regions analyzed by IHC; regions include the cingulate cortex/retrosplenial area (Ctx), hippocampus (Hipp), and entorhinal cortex/piriform area (Ent). Magnification of 100× microscopic images covering these brain regions was analyzed for post-synaptic biomarker (PSD95). 15 consecutive z-stack images were captured with ApoTome-equipped Zeiss microscope provided high-resolution images of synaptic puncta. (b) Quantitative analysis of PSD95<sup>+</sup> synaptic area assessed in Hipp, Ent, and combined brain regions in all experimental groups ( $n = 6-7$  mice/group). (c) Pearson's  $r$  correlation analysis between total brain PSD95<sup>+</sup> synaptic area and astrocytic marker glutamine synthetase (GS)<sup>+</sup> area per cell ( $n = 18$  mice). (d) Collective Pearson's  $r$  correlation of 6E10<sup>+</sup> Aβ-plaque burden against PSD95<sup>+</sup> post-synaptic density (black), GS<sup>+</sup> area/cell (brown), and GFAP<sup>+</sup> astrogliosis (green) in the Ent ( $n = 10-12$  mice). (e) Representative fluorescent images (40×) of coronal brain sections from Ent stained for astrocytes (GFAP, red), post-synaptic protein (PSD95, green), and cell nuclei (DAPI, blue) from PBS-control (top) and GA-immunized (bottom) old ADtg mice. (f) Representative, high-magnification images (100×) of a GA-immunized ADtg mouse brain showing density of PSD95 density. (g-h) Mass spectrometry analysis of total normalized peak protein area (TNPPA) of significantly changed synaptic proteins, including (g) synaptophysin and (h) synapsin-2, between all experimental groups ( $n = 4-6$  mice per group). (i) Heat map displaying relative fold change of significantly changed proteins in mass spectrometry analysis. Highlighted are AD-related amyloid-associated markers (amyloid-β A4 protein—APP/Aβ, clusterin—CLU, lysosomal-associated membrane protein 1 and 2—LAMP1/2) and inflammatory markers (glutamine synthetase—GS, intercellular adhesion molecule 1—ICAM1, h-2 class I histocompatibility antigen—HA11) that were significantly up- or down-regulated in brain and retinal tissues of PBS-control ADtg mice versus naïve WT mice and/or GA-immunized versus PBS-control ADtg mice ( $n = 4-6$  mice per group). Bar graphs indicate mean, standard error of mean (SEM), and individual data points. \* $p < 0.05$ , \*\* $p < 0.01$ , \*\*\* $p < 0.001$ , by one-way ANOVA with Tukey's post-test for three or more experimental groups. Mass spectrometry analysis by unpaired Student's  $t$  test. Pearson's  $r$  correlation analysis was used to determine statistical association



**TABLE 1** Quantitative mass spectrometry analysis of preselected proteins from brain and retinal tissue

Protein	Abbreviation	WT $\Xi$ ( $\pm$ SEM)	ADtg-PBS $\Xi$ ( $\pm$ SEM)	ADtg-GA $\Xi$ ( $\pm$ SEM)	FC ADtg vs. WT	P-value (t test)	FC GA vs. PBS	P-value (t test)
<b>Brain</b>								
Synaptic markers	Synaptophysin	5.6 ( $\pm$ 0.8)	2.7 ( $\pm$ 0.5)	4.4 ( $\pm$ 0.5)	0.48	<b>0.0288</b>	1.63	0.0611
	Synapsin-2	40.0 ( $\pm$ 2.6)	28.6 ( $\pm$ 5.3)	57.1 ( $\pm$ 7.3)	0.72	0.0655	2.00	<b>0.0218</b>
Inflammation	Glutamine synthetase	82.6 ( $\pm$ 5.4)	56.8 ( $\pm$ 10.9)	85.5 ( $\pm$ 6.8)	0.69	0.0536	1.51	<b>0.0390</b>
	Intercellular Adhesion Molecule 1	0.8 ( $\pm$ 0.1)	1.7 ( $\pm$ 0.2)	1.2 ( $\pm$ 0.2)	2.29	<b>0.0026</b>	0.70	0.1800
	H-2 Class I Histocompatibility Antigen	0.3 ( $\pm$ 0.02)	0.5 ( $\pm$ 0.1)	0.6 ( $\pm$ 0.04)	1.59	<b>0.0086</b>	1.05	0.7174
<b>Amyloid processing and clearance</b>								
Amyloid processing and clearance	Amyloid- $\beta$ A4 Protein	5.4 ( $\pm$ 0.5)	109.6 ( $\pm$ 33.2)	86.1 ( $\pm$ 14.8)	20.20	<b>&lt;0.0001</b>	0.79	0.4809
	Clusterin	13.6 ( $\pm$ 1.9)	71.7 ( $\pm$ 26.2)	36.8 ( $\pm$ 4.4)	5.27	<b>0.0237</b>	0.51	0.1423
	Lysosomal-Associated Membrane Protein 1	1.9 ( $\pm$ 0.2)	2.96 ( $\pm$ 0.3)	2.2 ( $\pm$ 0.1)	1.54	<b>0.0102</b>	0.73	<b>0.0037</b>
	Lysosomal-Associated Membrane Protein 2	2.5 ( $\pm$ 0.1)	3.3 ( $\pm$ 0.8)	2.6 ( $\pm$ 0.5)	1.34	<b>0.0287</b>	0.77	0.0787
<b>Retina</b>								
Inflammation	Glutamine synthetase	323.3 ( $\pm$ 30.1)	286.3 ( $\pm$ 13.4)	363.7 ( $\pm$ 32.5)	0.89	0.2419	1.27	<b>0.0001</b>
	Intercellular Adhesion Molecule 1	1.74 ( $\pm$ 0.1)	2.1 ( $\pm$ 0.1)	1.9 ( $\pm$ 0.1)	1.20	<b>0.0122</b>	0.92	0.2492
Inflammation	H-2 Class I Histocompatibility Antigen	0.5 ( $\pm$ 0.03)	0.7 ( $\pm$ 0.04)	0.6 ( $\pm$ 0.1)	1.27	<b>0.0101</b>	0.82	0.2914
	Amyloid processing and clearance	Amyloid- $\beta$ A4 Protein	3.1 ( $\pm$ 0.2)	10.9 ( $\pm$ 0.3)	9.6 ( $\pm$ 0.5)	3.47	<b>&lt;0.0001</b>	0.89
Inflammation	Clusterin	4.7 ( $\pm$ 0.2)	5.6 ( $\pm$ 0.3)	5.2 ( $\pm$ 0.3)	1.20	<b>0.0204</b>	0.93	0.3385
	Lysosomal-Associated Membrane Protein 1	1.1 ( $\pm$ 0.1)	1.3 ( $\pm$ 0.2)	1.1 ( $\pm$ 0.1)	1.18	0.4068	0.87	0.5359
	Lysosomal-Associated Membrane Protein 2	7.3 ( $\pm$ 0.3)	8.0 ( $\pm$ 0.3)	7.1 ( $\pm$ 0.1)	1.10	0.0965	0.89	<b>0.0287</b>

Data table includes analysis of PBS-control, GA-immunized, and WT naive experimental groups ( $n = 5-7$  mice/group). Protein peak areas were normalized to the total protein peak area of the respective sample and subjected to one-sample  $t$  tests to compare relative protein peak areas between the respective sample groups.  $t$  test  $p$ -value smaller than 0.05 and fold change  $\pm 1.2$  was highlighted as differentially expressed proteins.  $\Xi$ —Average of total normalized protein peak area ( $\times 10^5$ ).



Further, to explore effects of GA immunization on retinal and brain tissues from old, late-stage ADtg mice, a sensitive and quantitative MS proteomic analysis was applied (Figure 5g–i and Table 1; the complete MS datasets of identified proteins are included in Table S1 for brain and Table S2 for retina). The MS data revealed a reduction of cerebral presynaptic synaptophysin and synapsin-2 levels in PBS-control ADtg vs naïve WT mice ( $p = 0.0303$  and  $p = 0.0655$ , respectively, by one-way ANOVA; Figure 5g–h). Importantly, in accordance with histological findings of postsynapses, a significant increase in levels of synapsin-2 and a trend of elevation for synaptophysin were observed for GA-immunized versus PBS-control ADtg mice ( $p = 0.0112$  and  $p = 0.0611$ , respectively, by one-way ANOVA; Figure 5g–h).

## 2.7 | Cerebral and retinal AD-related protein profiles in response to immunomodulation

Next, proteins associated with amyloid, processing, clearance, and inflammation that were similarly and significantly down- or up-regulated in brain and retinal tissues from old mice either in disease or following GA immunization, as determined by MS analysis, are highlighted in Figure 5i. Specifically, parallels between brain and retinal proteins are shown by fold changes for the comparisons of PBS-control ADtg to naïve WT groups and GA-immunized to PBS-control ADtg groups (Figure 5i heatmaps; proteins up-regulated in red and down-regulated in blue; extended data with the statistical analyses shown in Table 1). Brain MS data revealed elevated GS concentrations in GA-immunized versus PBS-control ADtg mice (51% increase and  $p = 0.0390$ ; Table 1), which were remarkably normalized to levels observed in the WT mice. This response in GS astrocytic function following GA was mirrored in the retina, demonstrates another linkage between these two tissues (27% increase and  $p = 0.0001$ ; Table 1). Compared to WT, the immune markers intercellular adhesion molecule 1 (ICAM1), involved in T cell-APC adhesion, and the mouse MHC molecule H-2 class 1 histocompatibility complex (HA11) were increased in ADtg mouse brains (129% increase and  $p = 0.0026$ , 59% increase and  $p = 0.0086$ , respectively) and retina (20% increase and  $p = 0.0122$ , 27% increase and  $p = 0.0101$ , respectively; Figure 5i heatmaps and Table 1). However, the effects of GA did not reach statistical significance in both tissues.

In the context of amyloid processing and clearance, our quantitative MS analysis of cerebral and retinal APP/A $\beta$  further confirmed substantial increases with disease, albeit six times greater in the brain versus the retina (20-fold vs. 3.5-fold increases, respectively,  $p < 0.0001$ ; Figure 5i heatmaps and Table 1). Importantly, retinal APP/A $\beta$  protein levels in ADtg mice were significantly reduced by GA treatment (11% and  $p = 0.0396$ ; Table 1). The A $\beta$ -related clusterin chaperone protein (CLU) showed substantial increases in cerebral concentration in old ADtg vs WT mice (~5-fold increase and  $p = 0.0237$ ) and to a lesser but significant extent in the retina (20% increase and  $p = 0.0204$ ). Finally, two lysosomal-associated membrane proteins 1 and 2 (LAMP1/2) were similarly but to a lesser

extent affected by disease and GA immunization in the retina versus the brain. LAMP1 and LAMP2 were significantly elevated in ADtg versus WT mouse brains (54% increase and  $p = 0.0102$ , 34% increase and  $p = 0.0287$ , respectively), but did not reach statistical significance in the retina ( $p = 0.4068$  and  $p = 0.0965$ , respectively). Interestingly, GA immunomodulation primarily affected LAMP1 in the brain (27% decrease and  $p = 0.0037$ ) and LAMP2 in the retina (11% decrease and  $p = 0.0287$ ).

## 3 | DISCUSSION

This study provides the first evaluation of amyloidogenic and non-amyloidogenic A $\beta$  peptide levels and A $\beta_{42/40}$  ratios in paired retina and brain tissues from two cohorts of old, late-stage ADtg mice, including in response to immunomodulation. Our findings demonstrated the potential of the neurosensory retina to predict cerebral A $\beta$  accumulation in disease and following intervention in old ADtg mice, a more relevant model for the age-dependent human disease. Therapeutic effects of GA immunization in old age were revealed on both retinal and cerebral tissues. Further, we identified lateralization of A $\beta_{42}$ , A $\beta_{40}$ , A $\beta_{38}$  levels and A $\beta_{42/40}$  ratios between OS and OD retinae and between left and right brain hemispheres. While significant disparities in accumulation of A $\beta$  alloforms between left and right sides of these CNS tissues are detected, levels of A $\beta$  in one side consistently correlated with A $\beta$  levels in the respective side. Moreover, A $\beta_{40}$  burden strongly predicted A $\beta_{42}$  burden in each retina or brain tissue. Furthermore, our data found therapeutic effects of GA immunomodulation at advanced disease stages, as indicated by: (1) cerebral A $\beta$ -plaque reduction, especially targeting large and dense-core parenchymal deposits; (2) decreased cerebral vascular amyloidosis; (3) reduced A $\beta_{42}/A\beta_{40}$  ratio in the OD retina; (4) attenuation of cerebral GFAP<sup>+</sup>-astrocytosis and Iba1<sup>+</sup>-microgliosis; (5) enhanced cerebral Iba1<sup>hi</sup>/CD45<sup>hi</sup> myelomonocytic population surrounding A $\beta$  plaque; (6) preservation of synaptic integrity; and (7) restoration to homeostatic levels of several retinal and cerebral proteins related to astrocyte function, inflammation, and A $\beta$  processing and clearance, identified by MS proteomics profiling. Collectively, the multifaceted neuroprotection provided by GA immunization in old AD model mice suggests that CNS repair is possible via immunomodulation, even after severe tissue damage occurs. Further, the tight relationship between retinal and brain amyloidogenic A $\beta$  burden in response to immune-based treatment encourages future exploration of the retina as an advantageous AD biomarker for direct, noninvasive imaging to assess therapeutic efficacy.

The long-standing view of AD as a disease restricted to the brain has recently been challenged by mounting evidence supporting the manifestation of AD pathological hallmarks in the retina of animal models [reviewed in (Hart et al., 2016; Kusne et al., 2017; Mahajan & Votruba, 2017)] and human patients (Alexandrov et al., 2011; den Haan et al., 2018; Hadoux et al., 2019; Koronyo et al., 2017; Koronyo-Hamaoui et al., 2011; La Morgia et al., 2016; Schon et al., 2012; Schultz et al., 2020; Shi et al., 2020; Tsai et al., 2014). While



the retina is an appealing and accessible CNS organ for live imaging, the tissue's delicate and thin structure along with its small proportion in murine models raises particular technical challenges for *ex vivo* histological and biochemical assays. To overcome this hurdle, we developed an experimental protocol that allowed for quantitative measurements of neurosensory retinal peptides and proteins, including those with highly aggregative, amyloidogenic tendencies. This technique involved the separation of the neuro-retina from freshly dissected and snap-frozen eyes, concentration of tissue proteins, and subsequent denaturation of aggregates with epitope exposure by chemical conformational unraveling. Application of this method allowed for highly sensitive and quantitative triple-A $\beta$  alloform analyses by MSD assays.

Our study revealed for the first time an unexpected lateralization in A $\beta$  concentrations in OS versus OD retinae for A $\beta_{42}$ , A $\beta_{40}$ , and A $\beta_{38}$  alloforms, in addition to AD-relevant A $\beta_{42}$ /A $\beta_{40}$  ratio levels. Individual A $\beta$  alloforms were consistently and substantially higher in the OS compared with OD retina, with higher A $\beta_{42}$ /A $\beta_{40}$  ratios in the OD retina, indicating lateralization of A $\beta$  levels in the retina of these old, advanced-stage ADtg mice. Similarly, a previous study in AD human retina demonstrated lateralization in structural pathology, including RNFL thinning and tissue degeneration, with more pronounced pathology in the OS-left versus OD-right retina (Hwang et al., 2014). Importantly, our results of left posterior brain-dominant lateralization of A $\beta_{42/40}$  ratio is in agreement with previous studies in AD patients that identified left greater than right disease-associated cortical and white matter atrophy (Long et al., 2013; Mesulam et al., 2014; Minkova et al., 2017; Wahlund et al., 1993). In addition, AD patients have been reported to display reductions in left hemisphere glucose metabolism (Lehmann et al., 2013; Toga & Thompson, 2003; Weise et al., 2018), which has been associated with functional declines in verbal fluency (Weise et al., 2018). Other structural and molecular measurements also indicated lateralization between the two hemispheres, including a number of studies showing left-dominant accumulation of tauopathy, which could even predict disease onset (Mesulam et al., 2014; Minkova et al., 2017; Tetzloff et al., 2018; Wachinger et al., 2016). Most interestingly, in patients with right-hand dominance there was higher left-side brain tauopathy, while in patients with left-hand dominance and known right-hemisphere language dominance, tau burden lateralization shifted to the right hemisphere (Mesulam et al., 2014). Hence, it is postulated here that our findings of side-dominant susceptibility of A $\beta$  pathogenesis could be an outcome of differences in eye dominance, neuronal firing and circuit activity, and metabolism, eventually affecting A $\beta$  production, processing, propagation, or clearance processes.

Nevertheless, despite these disparities, there was a close linear correlation in levels of all A $\beta$  alloforms between the left and right retinae. In addition to having higher A $\beta$  peptide concentrations, the OS retina appears to better predict as compared to the OD retina its cerebral counterpart. If this disparity holds true in human patients, this may have implications in research methodologies and even organ acquisition. Additionally, results from prior investigations on retinal and brain pathology, averaging data from both eyes

and/or brain hemispheres, may be skewed. Future studies are warranted to establish retinal and brain A $\beta$ -burden lateralization and investigate the possible explanation of such lateralization in order to better understand processes regulating CNS A $\beta$  accumulation and removal.

While two previous reports have analyzed ocular A $\beta$  burden by ELISA in several transgenic murine AD models (Alexandrov et al., 2011; Parthasarathy et al., 2015; Schultz et al., 2020), they did not include analysis of paired retinas and brains, lateralization assessment, or they did not separate the neurosensory retina from other ocular tissues. Our previous investigations identified for the first time the presence of A $\beta$  plaques and characterized their morphology in retinas from AD patients and early-stage cases (Koronyo et al., 2017; Koronyo-Hamaoui et al., 2011; La Morgia et al., 2016; Shi et al., 2020). Moreover, our preliminary data detected a correlation between paired retinal A $\beta_{42}$ -containing plaques and cerebral plaque burden in these patients (Koronyo et al., 2017). In terms of retinal and brain response to therapy, reports in 12- and 14-month-old murine models of AD showed similar reductions in retinal and brain A $\beta$  plaques following immunization with dendritic cells loaded with MOG45D (Koronyo-Hamaoui et al., 2011) or with anti-A $\beta$  antibodies (Hwang et al., 2014; Liu et al., 2009). However, this was never precisely quantified by biochemical methods, nor measured specifically in old mice following GA immunization. Importantly, the feasibility to detect *in vivo* individual A $\beta$  plaque appearance and clearance dynamics in real time via a noninvasive retinal curcumin optical imaging method (Koronyo et al., 2012), and with aging (Sidiqi et al., 2020), encourages utilization of retinal amyloid imaging to gauge response to therapy with high spatial resolution. One limitation of this study is the lack of live retinal/brain imaging data to correlate with the histopathological findings. Our results rely on histological and biochemical analyses, revealing new phenomena that support the need to further correlate between live retinal/brain amyloid imaging and AD-related pathological biomarkers. Future investigation using live retinal imaging is warranted to identify such AD biomarkers, especially to facilitate evaluation of response to therapy.

The current studies led us to reveal the following fundamental unknowns regarding the potential connection between retinal and brain pathology in ADtg mice: (1) While the levels of retinal A $\beta_{38}$ , the more benign alloform, weakly corresponded to its left-posterior brain counterpart, the levels of retinal A $\beta_{40}$  and A $\beta_{42}$ , the synaptotoxic and AD-pathognomonic alloforms (Raskatov, 2019), tightly predicted the levels of their brain counterparts, especially following GA immunization, (2) As mentioned above, there were consistent disparities in accumulation of all A $\beta$  alloforms in left versus right retina and left versus right brain hemispheres, and (3) The therapeutic effects of GA immunomodulation were established at late-stage disease in the old ADtg mice, including notable parallels in molecular markers between retinal and cerebral tissues in disease and with therapy beyond A $\beta$  burden.

While non-significant small reductions were detected in cerebral A $\beta$  alloforms following GA immunization in old ADtg mice, GA did lead to substantial decreases in cerebral vascular and parenchymal



A $\beta$  plaques along with significant mitigations of microgliosis, astrocytosis, along with induction of homeostatic astrocyte profile. The measurement of A $\beta$  alloforms represents concentrations of both soluble and insoluble A $\beta$  forms, including the monomers, dimers, tetramers, oligomers, and other intermediates, which is beyond the plaques, and can explain the discrepancy between the histological and biochemical data. Moreover, the results of induced cerebral myeloid phagocytic cell recruitment and homing to the plaques sites may explain increased plaque clearance and synaptic preservation. Although one limitation of this study is the lack of cognitive testing, which was due to enhanced frailty and attrition rate among these old ADtg mice, our results of pre- and post-synaptic preservation (e.g., PSD95, synaptophysin, synapsin-2), which are typically predictive of cognitive function (Ferreira et al., 2015; Shankar et al., 2008), may indeed reflect a functional preservation.

Interestingly, the strength of the association displayed here between the OS and OD retina in levels of pathognomonic A $\beta_{42}$  was very similar to those observed between the retinae (individually and together) and their cerebral counterparts. Moreover, we found in our old ADtg mouse cohorts that the ratio between A $\beta_{42}$  and A $\beta_{40}$ , which is another key measure of AD neuropathology (Rembach et al., 2014; Schindler et al., 2019), was tightly regulated and similar across brain and retinal tissues. Importantly, the only imbalance in A $\beta_{42/40}$  ratio that was found in the OD retina of old ADtg mice was restored to levels equal to other measured CNS tissues by GA. The A $\beta_{42/40}$  ratio is thought to more accurately depict pathological burden and has been indicated in elevated protein toxicity when compared to single alloform levels alone (Kuperstein et al., 2010). This phenomenon may manifest as an OD-dominant lateralization in retinal and left-brain degenerative pathologies, which should be studied in future investigations. This result may also entail that despite differences in levels, the relative rates of A $\beta_{42}$  and A $\beta_{40}$  accumulations, affected by production and clearance, either in the retina or brain, are tightly connected, and potentially gives insight into another aspect of GA therapeutic impact.

In this study, we found that the concentrations of each A $\beta$  alloform are substantially lower in the retina than in the brain, which is in accordance with previously published results in animal models and human donors (Alexandrov et al., 2011; Grimaldi et al., 2018; Koronyo et al., 2017; Koronyo-Hamaoui et al., 2011; Schultz et al., 2020; Shi et al., 2020). Of note, it is believed that the concentrations of A $\beta_{42}$  deemed detrimental or toxic to brain cells and can lead to LTP deficits are dose-dependent (Raskatov, 2019). Whether and how retinal concentrations translate to retinal cell toxicity and pathology warrant future investigation. Nonetheless, growing histological evidence, both in humans and animal models, shows that retinal A $\beta$  depositions are tightly associated with local neuronal dysfunction (ERG), RNFL loss, RGC degeneration, and general tissue atrophy (Asanad et al., 2019; Grimaldi et al., 2018; Hart et al., 2016; Huang et al., 2017; Ju et al., 2013; Koronyo et al., 2012, 2017; La Morgia et al., 2016; Lei et al., 2017; Ning et al., 2008). Future studies should establish the detrimental retinal A $\beta$  concentrations, assemblies, and topographical locations in AD.

Early retinal and cerebral vascular dysfunctions have been tightly correlated with cognitive impairments related to AD (Attems & Jellinger, 2004; Brenowitz et al., 2015; DeCarli et al., 2019; Liesz, 2019; O'Bryhim et al., 2018; Querques et al., 2019; Shi et al., 2020; Thal et al., 2008). Our findings of substantial reduction of vascular entorhinal cortex deposits in the old GA-immunized ADtg mice should be clinically relevant since approximately 85 and 90% of AD patients also present with CAA (Brenowitz et al., 2015; Thal et al., 2002, 2008). The latter may be the result of deficiencies in A $\beta$  clearance through the blood-brain barrier (BBB; Bourassa et al., 2019; Hecht et al., 2018). Recent studies in human patients and animal models have demonstrated that amyloid deposition in vessels reduced blood flow and was associated with various other BBB and blood-retina barrier (BRB) dysfunctions, PDGFR $\beta$  down-regulation, as well as pericyte loss (Deane et al., 2009; Kimbrough et al., 2015; Nation et al., 2019; Ramanathan et al., 2015; Schultz et al., 2018; Shi et al., 2020; Sweeney et al., 2018; Zlokovic, 2011). In addition, astrocytes and their projections, called astrocytic end feet, extend to the walls of blood vessels and are considered a pivotal component of the neurovascular unit (Liu et al., 2018; Verkhratsky & Nedergaard, 2018). Our data indicate that immunomodulation was able to substantially curb reactive astrocytosis even at such an advanced disease stage, conceivably having a positive effect on BBB integrity and A $\beta$  clearance. Notably, our measurements of astrocytic phenotype directly and strongly correlated with severity of vascular and parenchymal A $\beta$  pathology. Future studies should look more closely into vascular dysfunction in AD and specifically assess the integrity of BBB/BRB-related biomarkers including astrocytic end feet (e.g., aquaporin-4), to investigate potential roles in BBB/BRB and lymphatic/glymphatic A $\beta$  clearance processes.

Results from the current study, together with several previous reports in younger adult ADtg mice, establish the therapeutic prospective of GA immunization in preclinical models of AD (Bakalash et al., 2011; Baruch et al., 2015; Butovsky et al., 2006, 2007; Frenkel et al., 2005; Koronyo et al., 2015; Li et al., 2020; Rentsendorj et al., 2018). The combined evidence for curbing cerebral A $\beta$ -plaque burden led us to undertake in-depth analysis of plaque subtypes to determine which type is primarily targeted by this immunomodulatory approach. Our morphological assessment of Ent A $\beta$  deposits suggested that GA immunization in old mice was most effective in reducing the size and number of large and dense-core plaques. These plaque subtypes were previously implicated in triggering neuroinflammation and increased neurotoxicity (Busche et al., 2008; Koffie et al., 2009; Li et al., 2020; Rasmussen et al., 2017; Selkoe, 2008; Shankar et al., 2008; Wang et al., 2016). In this regard, peripherally derived myelomonocytes were shown to more effectively recognize and phagocytose plaques comprised of fibrillar A $\beta$  forms versus soluble oligomers (Bernstein, et al., 2014; El Khoury et al., 2007; Koronyo et al., 2015; Lebson et al., 2010; Michaud et al., 2013; Rentsendorj et al., 2018; Zuroff et al., 2017). Nonetheless, GA activation of macrophages also induced a more effective extracellular degradation and clearance of soluble and oligomeric A $\beta_{42}$  forms, thereby protecting neurite structures and synaptic density (Koronyo et al., 2015; Li et al., 2020). This effect on oligomers was not specifically assessed here. Our histological observations, however,



highlighted that in brains of GA-immunized mice, there was a spatial organization of astrocytes and microglia/macrophages surrounding A $\beta$  plaques that may enhance the physical barrier, better protect neuronal network, and improve A $\beta$  clearance. The organized appearance of GFAP<sup>+</sup> astrocytes is most probably due to less activated astrocytes in between plaques. Future studies of the possible effects of GA immunotherapy on brain and retinal oligomeric A $\beta$  burden and associated gliosis in old ADtg mice are warranted.

Among the novel molecular mechanisms of GA immunization identified here, we found that levels of brain and retinal glutamine synthetase were normalized to levels comparable to those found in healthy WT mice via immunohistochemistry and mass spectrometry. Astrocyte-associated GS plays a crucial role in the balance of extracellular-synaptic glutamate levels, converting its excess into glutamine, and is integral in the well-established tripartite synapse model [reviewed in (Liu et al., 2018; Rudy et al., 2015)] (Allen & Barres, 2009; Allen & Eroglu, 2017; Belanger et al., 2011; Danbolt, 2001). Hence, GA-induced restoration of GS physiological levels may explain reduced excitotoxicity and preserved synapses (Ortinski et al., 2010; Son et al., 2019; Tani et al., 2014). In accordance with our MS data, dysfunctions in glutamate recycling processes were implicated in AD and drastic declines in the excitatory amino acid transporter 1 (EAAT1) of astrocytes within human tissue and astrocytic cultures exposed to A $\beta$  oligomers have been reported (Huang et al., 2018; Zoia et al., 2004). Interestingly, GS immunoreactive area adjacent to plaques tightly associated with post-synaptic density, suggesting that restoration of GS expression to homeostatic WT levels in A $\beta$ -burdened brain regions could prevent synaptic loss. The re-establishment of resting astrocyte morphology by GA identified by GFAP and GS histological IHC patterns and MS analysis further supports therapeutic efficacy at advanced disease stage.

Our quantitative MS analysis also showed that both retinal and cerebral tissues in old ADtg mice displayed significant up-regulation of several inflammatory-related proteins such as ICAM1, an adhesion molecule found on antigen-presenting cells and pericytes which facilitates transport of innate immune cells across the BBB (Martens et al., 2020; Proebstl et al., 2012). These findings are in line with previous studies reporting up-regulation of cerebral ICAM1 in a number of AD transgenic models (Ferretti et al., 2016) and, moreover, correlations with A $\beta$  and tau pathology in human AD patients (Walker et al., 2017). Increased h-2 class I histocompatibility antigen (HA11) mouse MHC molecule further implies heightened immune signaling and involvement in retinas and brains of old AD model mice.

A number of markers for amyloid production and cellular processing were markedly increased in the old, late-stage ADtg mice. Clusterin (CLU; also named Apolipoprotein J) and amyloid- $\beta$  A4 protein, encompassing pre-processed APP and the various A $\beta$  alloforms, showed extensive increases in diseased brains and retinas, corroborating our MSD and IHC analyses of A $\beta$ . Consistent with previous results, the brain displayed a substantial increase in magnitude changes as compared to the retina (Koronyo et al., 2017; Koronyo-Hamaoui et al., 2011). Finally, the lysosomal-associated membrane protein 1/2 (LAMP1/2) molecules have also been implicated in the

degradation of A $\beta$  fibrils (Barrachina et al., 2006; Gurney et al., 2018) and were found to be up-regulated in brain and retinal tissues from old ADtg mice. In response to GA immunomodulation, we revealed a preferential down-regulation of LAMP1 in the brain and LAMP2 in the retina. Overall, GA restored these molecules to levels similar to those observed in the healthy WT mice.

The results from this study substantiate the versatile therapeutic effects of GA immunomodulation on cerebral and retinal tissues in advanced disease stage in old murine models of AD, a more clinically relevant animal model. A successful immunomodulation approach at such late-stage disease supports future exploration of such an immunomodulatory strategy for AD treatment. Importantly, the concentrations of AD-associated A $\beta_{40}$  and A $\beta_{42}$  in the retina predicted their levels in the brain, especially following GA immunization. The intriguing retinal and cerebral lateralization of A $\beta_{42}$ , A $\beta_{40}$ , and A $\beta_{38}$  alloforms and A $\beta_{42/40}$  in these old mice may lead to reveal the environmental conditions that impose greater susceptibility or protection to AD. Altogether, the correlation of AD-related pathology and response to therapy of the retina and brain encourages future development of noninvasive retinal biomarkers to detect and monitor therapeutic efficacy.

## 4 | EXPERIMENTAL PROCEDURES

### 4.1 | Mouse model and experimental groups

Double-transgenic mouse models for Alzheimer's disease from the B6.Cg-Tg (APP<sub>SWE</sub>, PS1 <sub>$\Delta$ E9</sub>) 85Dbo/Mmjax strain (Jackson Laboratory, MMRRC Stock #34832-JAX; ADtg,  $n = 14$ ) and their age- and gender-matched non-transgenic (WT,  $n = 7$ ) littermates (Cohort 1). Animals were aged until 20 months and then divided into three experimental groups in equal numbers ( $n = 7$ , 3F/4 M): naïve wild-type (WT), PBS-injected ADtg control and GA-immunized ADtg mice (Figure 1a–b). An additional cohort of double-transgenic mouse models for AD from the B6.Cg-Tg (APP<sub>SWE</sub>, PS1 <sub>$\Delta$ E9</sub>) 85Dbo/Mmjax strain (Jackson Laboratory, MMRRC Stock #34832-JAX; ADtg,  $n = 15$ ) were aged until an average age of 18 months (Cohort 2; 2F/13 M; Figure 1c). In general, this murine model displays an AD-like neuropathology and symptoms. Such neuropathies and behavioral changes include vast parenchymal and vascular A $\beta$  accumulation, both in its soluble and insoluble forms, astrocytic, microglial, and molecular inflammatory responses, in addition to synaptic loss and subsequent cognitive decline (Jankowsky et al., 2004; Meyer-Luehmann et al., 2008). This study was performed according to regulations of the Cedars-Sinai Medical Center Institutional Animal Care and Use Committee under an approved protocol.

### 4.2 | GA immunization and tissue allocation

ADtg mice from Cohort 1 were subcutaneously injected with 200  $\mu$ l of either PBS or 100  $\mu$ g glatiramer acetate (GA; also known as Copaxone<sup>®</sup>, TEVA Neuroscience) in PBS. Injections were administered twice a week for the first 2 weeks, then once a week for the





following 6 weeks—totaling 10 injections. A week after the completion of treatment period, WT and ADtg mice reached an average age of 22.4 months; they were euthanized with perfusion using ice-cold saline supplemented with 0.5 mM EDTA, as previously described (Koronyo et al., 2015). Brains right hemisphere were collected and fixed overnight in 2.5% paraformaldehyde (Sigma-Aldrich), then cryo-protected in 30% sucrose. The entirety of the right brain hemisphere was separated for immunohistochemistry analyses. The left posterior brain hemisphere (divided at Bregma -1 mm) was snap frozen for protein analyses and stored at -80°C. Eyes, Oculus Sinister (OS) and Oculus Dexter (OD), were flash-frozen in dry ice then stored at -80°C until retinal extraction and protein analyses. The experimental design and allocation of tissue for Cohort 1 are detailed in Figure 1a–b. At the average age of 18 month, Cohort 2 was euthanized and perfused under the same protocol described above. The left and right posterior brains, as well as both OS and OD retinae, were separated for protein analyses. All experiments were conducted and recorded by researchers blinded to the mouse genotypes and the treatment group. The experimental design and allocation of tissue for Cohort 2 are detailed in Figure 1c.

#### 4.3 | Retinal and brain protein isolation and processing for meso scale discovery (MSD)

Frozen mice eyeballs were placed in a cold solution of 1% Protease Inhibitor in PBS whereupon the cornea and iris were separated, and lens extracted along with the vitreous, being careful not to damage the retina. Using a pair of forceps, the retina was carefully detached from the sclera and snipped at the base of the optic nerve. The retinal weight was recorded and tissue subsequently frozen on dry ice. Posterior brain tissues were separated, weight was recorded, and frozen on dry ice. A lysis buffer containing 0.15 M NaCl, 1 mM Ethylenediaminetetraacetic acid/EDTA, 1% Triton X, and 1% Protease Inhibitor was added to each retina and brain tissue and homogenized via rod sonication (4 Hz; for two cycles of 1.5 min in 15-s increments). The homogenized tissue, including soluble and insoluble fractions, was then placed into a Speed Vac Concentrator for 3.5 h. The remaining lyophilized tissue pellet was resuspended in a solution of >99% hexafluoroisopropanol (HFIP; Sigma), then homogenized via rod sonication (4 Hz; for 1 cycles of 1.5 min in 15-s increments) and left overnight (12 h) unraveling the aggregated amyloidogenic proteins for more accurate and sensitive detection. After evaporation of the HFIP, the pellet was resuspended in sterile PBS following homogenized via rod sonication (4 Hz for 1 cycles of 1.5 min in 15-s increments) and used to determine the protein levels of A $\beta$ <sub>42</sub>, A $\beta$ <sub>40</sub>, and A $\beta$ <sub>38</sub> by Meso Scale Discovery (MSD; #K15199G-1). A schematic illustration of this protocol is shown in Figure 1d. For data regarding both retinae, an average of the OS and the OD retinal values was obtained and designated as “Both” for each mouse individually.

#### 4.4 | Immunohistochemistry (IHC)

Mouse right brain hemispheres from Cohort 1 were coronally sectioned into 30- $\mu$ m thick slices and stored in a 0.01% solution of sodium azide (NaN<sub>3</sub>) in PBS. Brain sections were washed in PBS then incubated in blocking buffer (Dako #X0909), followed by primary antibody incubation overnight in 4°C with combinations of the following primary antibodies in 10% blocking buffer (3–6 sections/mouse): mouse anti-human A $\beta$  [residues 1–16, mAb clone 6E10 (1:200; #803001; BioLegend), and residues 17–24, mAb clone 4G8 (1:200; #800701; BioLegend)], rabbit anti-glia fibrillary acidic protein (GFAP) pAb (1:100; G9269; Sigma-Aldrich), rat anti-GFAP mAb (1:1,000; #13-0300; Thermo Fisher), mouse anti-Glutamine Synthetase mAb (1:200; SC-74430; Santa Cruz Biotechnology), rabbit anti-PSD95 mAb (1:600; ab76115; Abcam), guinea pig anti-VGluT1 pAb (1:6,000; AB5905; Millipore), goat anti-Iba1 pAb (1:500; NB100-1028; NovusBio), rabbit anti-Iba1 pAb (1:200; #019-19741, Wako Chemicals USA), rat anti-CD45 mAb (1:25; #550539; BD PharMingen). Sections were then washed in PBS before incubation at 37°C for 1 h with secondary polyclonal antibodies (donkey anti-mouse, anti-rat, anti-goat, anti-guinea pig, and anti-rabbit; 1:200; Jackson ImmunoResearch Laboratories) conjugated with Cy2, Cy3, Cy5, or DyLight™ 649. Sections were finally washed in PBS then mounted using ProLong® Gold antifade reagent with DAPI (Molecular Probes, Life Technologies). Routine negative controls for IHC assessments were processed using the same immunolabeling protocol with the omission of the primary antibody to assess non-specific signal. “Serial brain sections” are defined as separated by five slices. Images were repeatedly captured at the same focal planes with the same exposure time using a Carl Zeiss Axio Imager Z1 fluorescence microscope (Carl Zeiss MicroImaging, Inc.) equipped with ApoTome, AxioCam MRm, and AxioCam HRc cameras. Images were captured at 20 $\times$ , 40 $\times$ , 63 $\times$ , and 100 $\times$  objectives for different purposes.

#### 4.5 | GS mouse-on-mouse peroxidase staining

For mouse primary GS anti-mouse antibodies, a Vector® M.O.M.™ (mouse-on-mouse) immunodetection kit (BMK-2202, Vector Laboratories) was used to reduce non-specific auto-reactivity of endogenous proteins. Briefly, sections were incubated in 3% hydrogen peroxide for 10 min at room temperature in order to block endogenous peroxidase activity (3 sections/mouse). A M.O.M IgG Blocking Reagent was applied for 1 h at room temperature. Afterward, sections were left in M.O.M. Diluent for 5 min. GS anti-mouse primary antibody was diluted (1:200) in M.O.M. Diluent solution and incubated with tissue for 30 min at room temperature. Anti-mouse IgG M.O.M. Biotinylated reagent in M.O.M. Diluent was applied at room temperature for 10 min before a Vectastain ABC reagent (Vector, PK-6102, Peroxidase Mouse IgG) was applied. Subsequently, 3,3'-diaminobenzidine (DAB) in chromogen



solution (Dako K3468) was added for visual detection by nonfluorescent immunoperoxidase.

#### 4.6 | CAA scoring

For amyloid burden assessment in mouse brain vasculature, sections were stained with 6E10 (1:200; #803001; BioLegend) according to a previously described standard protocol (Koronyo-Hamaoui et al., 2020; Rentsendorj et al., 2018). Various degrees of cerebral amyloid angiopathy (CAA) in animals were defined by analyzing 6E10-labeled brain sections using a scale of 0–4 (0 indicates no CAA, 4 indicates severe CAA, detailed in Figure 3f; three brain sections per animal), as previously described (Wyss-Coray & Mucke, 2002). We scored three sections (~10 vessels per image) per animal spanning a 2.25 mm<sup>2</sup> area of the entorhinal cortex per mouse. These scores were averaged per mouse and compared between PBS-control and GA-treated groups.

#### 4.7 | Amyloid plaque size determination

The number and area ( $\mu\text{m}^2$ ) of 6E10<sup>+</sup> A $\beta$  plaques were determined by examining three coronal sections per mouse spanning the entorhinal cortex region. Five images were taken per section at 20 $\times$  magnification, and each image was analyzed using Carl Zeiss AxioVision LE software (Carl Zeiss MicroImaging, Inc.). 6E10<sup>+</sup> A $\beta$  plaques were individually traced using the “outline” and “length” tool for measurements of area, length (longest diameter), and width (shortest diameter). Each plaque was morphologically assessed as either a Dense-Core plaque, if its core was intensely labeled and clear, or a Non-Dense-Core plaque. After analysis of all mouse brain sections, the criteria for Large, Medium, Small, and X-Small plaques were defined by combining the range of measurements obtained in each category (area: 24.13–11,509.33  $\mu\text{m}^2$ , length: 5.64–143.5  $\mu\text{m}$ , and width: 5.56–95.66  $\mu\text{m}$ ) and observational assessment per image. The criteria were as follows: large area = >1,000  $\mu\text{m}^2$ , length = >50  $\mu\text{m}$ , width = >30  $\mu\text{m}$ ; medium area = 400–1,000  $\mu\text{m}^2$ , length = 30–50  $\mu\text{m}$ , width = 20–30  $\mu\text{m}$ ; small area = 100–400  $\mu\text{m}^2$ , length = 15–30  $\mu\text{m}$ , width = 10–20  $\mu\text{m}$ ; extra-small area = <100  $\mu\text{m}^2$ , length = <15  $\mu\text{m}$ , width = <10  $\mu\text{m}$  (detailed in Figure 3h). We covered a total of 2.25 mm<sup>2</sup> area per mouse brain, and mean values were calculated as the average of 15 images, each spanning 1.5  $\times$  105  $\mu\text{m}^2$  area. Analyzers were blinded to the mouse groups when performing all counts.

#### 4.8 | Synaptic quantification

For synaptic analysis and to cover the entorhinal cortex/piriform area, three of the same rectangular fields (90  $\mu\text{m}$   $\times$  70  $\mu\text{m}$ ) under 100 $\times$  oil objective lens were precisely selected in the lateral and

medial blade molecular layer (ML) of the dentate gyrus (DG), the stratum lacunosum-moleculare (SLM), the stratum radium (SR), and the stratum oriens (SO) of cornu ammonis 1 (CA1) in each condition, respectively. In addition, three of the same fields were carefully chosen in layers 2 and 3 of the entorhinal cortex. Fifteen optical sections per field, nine fields per hippocampal area, six fields per entorhinal cortex/piriform area, five fields per cingulate cortex/retrosplenial area per section, and 300 total images per brain were analyzed. Single optical section images at 0.25  $\mu\text{m}$  intervals and 3.75  $\mu\text{m}$  Zeiss ApoTome high-resolution scans were performed. Synaptic puncta number and synaptic immunoreactive (IR) area were quantified using Puncta Analyzer 2, 3, and ImageJ (NIH) macro and batch process. Average synaptic area was calculated for each condition.

#### 4.9 | Sample preparation for mass spectrometry analysis

The protein lysates from brains and retinae were subjected to detergent removal process using detergent removal spin column (Pierce<sup>™</sup>, Thermo Scientific) as per manufacturer's instructions. Post-detergent removal, protein amounts were quantified using BCA assay (Pierce<sup>™</sup>, Thermo Scientific) as per manufacturer's instructions and an equal amount of (50  $\mu\text{g}$ ) proteins per samples were subjected to reduction with 10 mM dithiothreitol (DTT) followed by alkylation with 20 mM iodoacetamide (IAA) in the dark. Finally, the reaction was quenched with excess DTT for 15 min. Proteins were digested at 37°C overnight with trypsin at a 1:50 ratio (enzyme to protein ratio). The digests were quenched with formic acid, and peptides were desalted using self-packed SDB-RP StageTips (Empore SPE disks) and dried in vacuum centrifuge. Peptide concentration was determined using peptide BCA assay kit as per manufacturer's instructions.

#### 4.10 | Peptide ion library generation

To produce a peptide ion library of relevant proteins, a pool of peptides was prepared individually for brain and retina sample peptides by mixing equal amounts of respective samples. This identified a base list of proteins from which a subset was chosen that were related to previous IHC analyses. Samples were desalted with C18 Sep Pack Light Cartridges (Waters, USA) and dried down using vacuum centrifugation. Peptides were reconstituted with 5 mM ammonia solution (pH 10.5) and loaded onto an Agilent 300 Extend C18 column (2.1 mm  $\times$  150 mm, 3.5  $\mu\text{m}$ , 300 Å). Using a 1,260 quaternary HPLC system, peptides were separated using a linear gradient of 5 mM ammonia solution with 90% acetonitrile (pH 10.5) starting from 3 to 30% for 55 min at a flow rate of 300  $\mu\text{l}/\text{min}$ . Peptides were separated into a total of 90 fractions that were consolidated into 17 for liquid chromatography tandem mass spectrometry (IDA-LC-MS/MS) analysis.



#### 4.11 | Information-dependent acquisition mass spectrometry (IDA-MS)

A 6,600 TripleTOF mass spectrometer (Sciex) coupled to an Eksigent Ultra-nano-LC-1D system (Eksigent, Sciex) was employed for both IDA and SWATH-MS analysis. HpH fractionated peptide was subjected to 1D-IDA nano-LC MS/MS analysis (IDA-LC-MS/MS) as follows. Each sample was injected onto a reverse-phase trap for pre-concentration. The peptide trap (solid core Halo-C18, 160 Å, 2.7 µm, 100 µm × 3.5 cm) was then switched into line with the analytical column (solid core Halo-C18, 160 Å, 2.7 µm, 200 µm × 20 cm). Peptides were eluted from the column using a linear solvent gradient of 2 and 30% of mobile phase B over 88 min at a flow rate of 600 nL/min. The reverse-phase nano-LC eluent was subject to positive ion nano-flow electrospray analysis in an information-dependent acquisition (IDA) mode. First, a TOF-MS survey scans were acquired ( $m/z$  350–1,500, 0.25 s) with the 20 most intense multiple charged ions (2+ to 5+; exceeding 200 counts per second) in the survey scan being sequentially subjected to MS/MS analysis. MS/MS spectra were accumulated for 100 ms in the mass range  $m/z$  100–1,800 using rolling collision energy.

#### 4.12 | Data independent acquisition using SWATH mass spectrometry (SWATH-MS)

Protein quantification using SWATH-MS was performed as described by Kamath et al (<https://pubs.acs.org/doi/10.1021/acs.jproteome.7b00561>) with modification. Briefly, equal amounts of individual samples (approximately 2 µg) were separated over reverse-phase linear gradient of 2 and 35% of mobile phase B over 88 min at a flow rate of 600 nL/min using the same LC and MS instruments as specified above with positive nano-flow electrospray mode. In SWATH mode, first a TOF-MS survey scan was acquired ( $m/z$  350–1,500, 0.05 s), and then, the 100 predefined  $m/z$  ranges were sequentially subjected to MS/MS analysis. MS/MS spectra were accumulated for 30 ms in the mass range  $m/z$  350–1,500 with rolling collision energy optimized for lowed  $m/z$  in  $m/z$  window +10%. To minimize instrument condition caused bias, SWATH data for each sample were acquired in a random order with one blank injection acquired between every sample injection.

#### 4.13 | Mass spectrometry data analysis

IDA-MS data analysis and ion library generation are as follows. Respective IDA-MS data files for brain and retina samples were consolidated and searched with ProteinPilot (v5.0, Sciex) using the Paragon™ algorithm in thorough mode. UniProt Mus musculus proteome database was used and searched using a tolerance of 2 missed tryptic cleavages. Fixed modifications were set for carbamidomethylation of cysteine. An Unused Score cutoff was set to 1.3 (95% confidence for identification). Resultant two data files were

utilized as spectral/ion library for SWATH-MS data analysis. Mass spectrometry data for both brain and retina samples were analyzed using a threshold of 1.2 fold change. Among the remaining list of proteins present in both retina and brain, specific AD proteins of interest were further highlighted (Table 1), and only if they were down-regulated or up-regulated significantly in either brain or retina of ADtg mice relative to WT and restored either partially or fully to WT levels by GA treatment. A complete list of significantly identified proteins for brains (Table S1) and retina (Table S2) display fold change and comparisons between WT naïve and PBS control, as well as GA-immunized and PBS control.

#### 4.14 | SWATH-MS data analysis

Both Ion library and SWATH-MS data files were imported into PeakView software 2.1 using the SWATH MicroApp 2.0 (SCIEX), and data were extracted using the following parameters: Top 6 most intense fragments of each peptide were extracted from the SWATH data sets (75 ppm mass tolerance, 5 min retention time window). Modified and shared peptides were excluded from quantification. After data processing, peptides (max 100 peptides per protein) with confidence >99% and FDR <1% (based on chromatographic feature after fragment extraction) were used for the quantitation. Cumulative protein areas from extracted ion chromatograms were exported to Excel for further analysis. The protein peaks areas were normalized to the total protein peak area of the respective sample and subjected to one-sample  $t$  tests to compare relative protein peak areas between the respective sample groups.  $t$  test  $p$ -value smaller than 0.05 and fold change  $\pm 1.2$  was highlighted as differentially expressed proteins. Two approaches were considered for determining differential expression: ANOVA on the log-transformed normalized protein peak areas of all samples and  $t$  test pairwise comparisons of pairs of specific samples. For the analysis of variance, proteins were deemed to be differentially expressed if the ANOVA  $p$ -value was less than 0.05 and the maximum protein fold change exceeded 1.2.

#### 4.15 | Statistical analysis

Data were analyzed using GraphPad Prism 6.01 (GraphPad Software). A two-tailed unpaired Student's  $t$  test was applied for analytic comparisons between two groups. Comparison of three or more groups was performed using one-way ANOVA with Tukey's multiple comparison post-test of paired groups. Analysis of two independent variables was performed using two-way ANOVA with Sidak's post-test. Correlation analysis was performed using Prism Pearson's tests. Results are expressed as means  $\pm$  standard deviations (SDs) or means  $\pm$  standard errors of the mean (SEMs) as indicated. A  $p$ -value <0.05 was considered significant, and a  $p$ -value <0.10 was regarded as a trend.



## ACKNOWLEDGMENTS

The authors thank Mia Oviatt for help with editing. This article is dedicated to the memory of Dr. Salomon Moni Hamaoui and Lillian Jones Black, both of whom died from Alzheimer's disease. This work was supported by the National Institutes of Health (NIH) NIA R01AG056478 and NIA R01AG055865 Awards (MKH), The Saban, The Maurice Marciano, and The Tom Gordon Private Foundations (MKH). The authors also acknowledge the funding support from the National Health and Medical Research Council (NHMRC), Petersen Foundation (PKS), Australian Government's National Collaborative Research Infrastructure Scheme (NCRIS; MM) and Macquarie University (VKG, SLG, MM). This work was supported by the National Institutes of Health (NIH) NIA R01AG056478 and NIA R01AG055865 Awards (MKH), The Saban, The Maurice Marciano, and The Tom Gordon Private Foundations (MKH).

## CONFLICT OF INTEREST

Y.K., M.K.H., and K.L.B. are co-founders and stockholders of NeuroVision Imaging, Inc., 1395 Garden Highway, Suite 250, Sacramento, CA 95833, USA.

## AUTHORS' CONTRIBUTIONS

Study design: Maya Koronyo-Hamaoui, Jonah Doustar, Yosef Koronyo; Acquisition of data: Jonah Doustar, Altan Rentsendorj, Tania Torbati, Giovanna C. Regis, Dieu-Trang Fuchs, Julia Sheyn, Nazanin Mirzaei, Mitra Mastali, Yosef Koronyo, Maya Koronyo-Hamaoui; MSD analysis: Mitra Mastali, Jonah Doustar, Yosef Koronyo, Julia Sheyn, Jennifer E. Van Eyk, Maya Koronyo-Hamaoui; Mass spectrometry: Vivek K. Gupta, Stuart L. Graham, Nazanin Mirzaei; Analysis and interpretation of data: Jonah Doustar, Altan Rentsendorj, Giovanna C. Regis, Tania Torbati, Nazanin Mirzaei, Dieu-Trang Fuchs, Julia Sheyn, Mitra Mastali, Yosef Koronyo, Maya Koronyo-Hamaoui; Statistical analysis: Jonah Doustar, Altan Rentsendorj, Giovanna C. Regis, Tania Torbati, Dieu-Trang Fuchs, Julia Sheyn, Nazanin Mirzaei, Mitra Mastali, Maya Koronyo-Hamaoui; Drafting of manuscript: Maya Koronyo-Hamaoui, Jonah Doustar, Tania Torbati, Giovanna C. Regis; Manuscript editing: Maya Koronyo-Hamaoui, Jonah Doustar, Tania Torbati, Altan Rentsendorj, Giovanna C. Regis, Dieu-Trang Fuchs, Mitra Mastali, Yosef Koronyo, Maya Koronyo-Hamaoui; Discussion of results: Maya Koronyo-Hamaoui, Jonah Doustar, Altan Rentsendorj, Tania Torbati, Giovanna C. Regis, Yosef Koronyo, Stuart L. Graham, Vivek K. Gupta, Keith L. Black, Prediman K. Shah, Nazanin Mirzaei; Study conception and supervision: Maya Koronyo-Hamaoui. All authors read and approved the final manuscript.

## DATA AVAILABILITY STATEMENT

The datasets used and/or analyzed during the current study are available from the corresponding author on reasonable request. All experimental materials are commercially available and specified in the methods section.

## ORCID

Jonah Doustar  <https://orcid.org/0000-0002-3029-0067>

Tania Torbati  <https://orcid.org/0000-0002-9409-791X>

Giovanna C. Regis  <https://orcid.org/0000-0003-3606-3882>

Nazanin Mirzaei  <https://orcid.org/0000-0002-5753-5300>

Stuart L. Graham  <https://orcid.org/0000-0001-7519-969X>


Prediman K. Shah  <https://orcid.org/0000-0002-6351-8291>

Mitra Mastali  <https://orcid.org/0000-0002-9988-092X>

Jennifer E. Van Eyk  <https://orcid.org/0000-0001-9050-148X>

Keith L. Black  <https://orcid.org/0000-0002-0546-4934>

Mehdi Mirzaei  <https://orcid.org/0000-0001-8727-4984>

Maya Koronyo-Hamaoui  <https://orcid.org/0000-0003-2864-8442>

## REFERENCES

- Alexandrov, P. N., Pogue, A., Bhattacharjee, S., & Lukiw, W. J. (2011). Retinal amyloid peptides and complement factor H in transgenic models of Alzheimer's disease. *NeuroReport*, 22(12), 623–627.
- Allen, N. J., & Barres, B. A. (2009). Neuroscience: Glia—More than just brain glue. *Nature*, 457(7230), 675–677. <https://doi.org/10.1038/457675a>
- Allen, N. J., & Eroglu, C. (2017). Cell biology of astrocyte-synapse interactions. *Neuron*, 96(3), 697–708. <https://doi.org/10.1016/j.neuron.2017.09.056>
- Alzheimer's Association. (2018). 2018 Alzheimer's disease facts and figures. *Alzheimer's & Dementia*, 14(3), 367–429. <https://doi.org/10.1016/j.jalz.2018.02.001>
- Asanad, S., Ross-Cisneros, F. N., Barron, E., Nassisi, M., Sultan, W., Karanjia, R., & Sadun, A. A. (2019). The retinal choroid as an oculo-vascular biomarker for Alzheimer's dementia: A histopathological study in severe disease. *Alzheimer's & Dementia: the Journal of the Alzheimer's Association*, 11, 775–783. <https://doi.org/10.1016/j.jadadm.2019.08.005>
- Attems, J., & Jellinger, K. A. (2004). Only cerebral capillary amyloid angiopathy correlates with Alzheimer pathology—a pilot study. *Acta Neuropathologica*, 107(2), 83–90. <https://doi.org/10.1007/s00401-003-0796-9>
- Bakalash, S., Pham, M., Koronyo, Y., Salumbides, B. C., Kramerov, A., Seidenberg, H., Berel, D., Black, K. L., & Koronyo-Hamaoui, M. (2011). Egr1 expression is induced following glatiramer acetate immunotherapy in rodent models of glaucoma and Alzheimer's disease. *Investigative Ophthalmology & Visual Science*, 52(12), 9033–9046. <https://doi.org/10.1167/iovs.11-7498>
- Barrachina, M., Maes, T., Buesa, C., & Ferrer, I. (2006). Lysosome-associated membrane protein 1 (LAMP-1) in Alzheimer's disease. *Neuropathology and Applied Neurobiology*, 32(5), 505–516. <https://doi.org/10.1111/j.1365-2990.2006.00756.x>
- Baruch, K., Rosenzweig, N., Kertser, A., Deczkowska, A., Sharif, A. M., Spinrad, A., Tsitsou-Kampeli, A., Sarel, A., Cahalon, L., & Schwartz, M. (2015). Breaking immune tolerance by targeting Foxp3+ regulatory T cells mitigates Alzheimer's disease pathology. *Nature Communications*, 6, 7967. <https://doi.org/10.1038/ncomms8967>
- Belanger, M., Allaman, I., & Magistretti, P. J. (2011). Brain energy metabolism: Focus on astrocyte-neuron metabolic cooperation. *Cell Metabolism*, 14(6), 724–738. <https://doi.org/10.1016/j.cmet.2011.08.016>
- Benilova, I., Karran, E., & De Strooper, B. (2012). The toxic Abeta oligomer and Alzheimer's disease: An emperor in need of clothes. *Nature Neuroscience*, 15(3), 349–357. <https://doi.org/10.1038/nn.3028>
- Bernstein, K. E., Gonzalez-Villalobos, R. A., Giani, J. F., Shah, K., Bernstein, E., Janjulia, T., Koronyo, Y., Shi, P. D., Koronyo-Hamaoui, M., Fuchs, S., & Shen, X. Z. (2014). Angiotensin-converting enzyme overexpression in myelocytes enhances the immune response.



- Biological Chemistry*, 395(10), 1173–1178. <https://doi.org/10.1515/hsz-2013-0295>
- Bernstein, K. E., Koronyo, Y., Salumbides, B. C., Sheyn, J., Pelissier, L., Lopes, D. H. J., Shah, K. H., Bernstein, E. A., Fuchs, D.-T., Yu, J.-Y., Pham, M., Black, K. L., Shen, X. Z., Fuchs, S., & Koronyo-Hamaoui, M. (2014). Angiotensin-converting enzyme overexpression in myelomonocytes prevents Alzheimer's-like cognitive decline. *Journal of Clinical Investigation*, 124(3), 1000–1012. <https://doi.org/10.1172/JCI66541>
- Bourassa, P., Tremblay, C., Schneider, J. A., Bennett, D. A., & Calon, F. (2019). Beta-amyloid pathology in human brain microvessel extracts from the parietal cortex: Relation with cerebral amyloid angiopathy and Alzheimer's disease. *Acta Neuropathologica*, 137(5), 801–823. <https://doi.org/10.1007/s00401-019-01967-4>
- Bradshaw, E. M., Chibnik, L. B., Keenan, B. T., Ottoboni, L., Raj, T., Tang, A., Rosenkrantz, L. L., Imboya, S., Lee, M., Von Korff, A., Morris, M. C., Evans, D. A., Johnson, K., Sperling, R. A., Schneider, J. A., Bennett, D. A., & De Jager, P. L. (2013). CD33 Alzheimer's disease locus: Altered monocyte function and amyloid biology. *Nature Neuroscience*, 16(7), 848–850. <https://doi.org/10.1038/nn.3435>
- Brenowitz, W. D., Nelson, P. T., Besser, L. M., Heller, K. B., & Kukull, W. A. (2015). Cerebral amyloid angiopathy and its co-occurrence with Alzheimer's disease and other cerebrovascular neuropathologic changes. *Neurobiology of Aging*, 36(10), 2702–2708. <https://doi.org/10.1016/j.neurobiolaging.2015.06.028>
- Busche, M. A., Eichhoff, G., Adelsberger, H., Abramowski, D., Wiederhold, K.-H., Haass, C., Staufenbiel, M., Konnerth, A., & Garaschuk, O. (2008). Clusters of hyperactive neurons near amyloid plaques in a mouse model of Alzheimer's disease. *Science*, 321(5896), 1686–1689. <https://doi.org/10.1126/science.1162844>
- Butovsky, O., Koronyo-Hamaoui, M., Kunis, G., Ophir, E., Landa, G., Cohen, H., & Schwartz, M. (2006). Glatiramer acetate fights against Alzheimer's disease by inducing dendritic-like microglia expressing insulin-like growth factor 1. *Proceedings of the National Academy of Sciences USA*, 103(31), 11784–11789. <https://doi.org/10.1073/pnas.0604681103>
- Butovsky, O., Kunis, G., Koronyo-Hamaoui, M., & Schwartz, M. (2007). Selective ablation of bone marrow-derived dendritic cells increases amyloid plaques in a mouse Alzheimer's disease model. *European Journal of Neuroscience*, 26(2), 413–416. <https://doi.org/10.1111/j.1460-9568.2007.05652.x>
- Chang, L. Y., Ardiles, A. O., Tapia-Rojas, C., Araya, J., Inestrosa, N. C., Palacios, A. G., & Acosta, M. L. (2020). Evidence of synaptic and neurochemical remodeling in the retina of aging degus. *Frontiers in Neuroscience*, 14, 161. <https://doi.org/10.3389/fnins.2020.00161>
- Chiasseu, M., Alarcon-Martinez, L., Belforte, N., Quintero, H., Dotigny, F., Destroismaisons, L., Vande Velde, C., Panayi, F., Louis, C., & Di Polo, A. (2017). Tau accumulation in the retina promotes early neuronal dysfunction and precedes brain pathology in a mouse model of Alzheimer's disease. *Molecular Neurodegeneration*, 12(1), 58. <https://doi.org/10.1186/s13024-017-0199-3>
- Chiti, F., & Dobson, C. M. (2017). Protein misfolding, amyloid formation, and human disease: A summary of progress over the last decade. *Annual Review of Biochemistry*, 86, 27–68. <https://doi.org/10.1146/annurev-biochem-061516-045115>
- Danbolt, N. C. (2001). Glutamate uptake. *Progress in Neurobiology*, 65(1), 1–105.
- De Strooper, B., & Karran, E. (2016). The cellular phase of Alzheimer's disease. *Cell*, 164(4), 603–615. <https://doi.org/10.1016/j.cell.2015.12.056>
- Deane, R., Bell, R. D., Sagare, A., & Zlokovic, B. V. (2009). Clearance of amyloid-beta peptide across the blood-brain barrier: Implication for therapies in Alzheimer's disease. *CNS & Neurological Disorders: Drug Targets*, 8(1), 16–30.
- DeCarli, C., Villeneuve, S., Maillard, P., Harvey, D., Singh, B., Carmichael, O., Fletcher, E., Olichney, J., Farias, S., Jagust, W., Reed, B., & Mungas, D. (2019). Vascular burden score impacts cognition independent of amyloid PET and MRI measures of Alzheimer's disease and vascular brain injury. *Journal of Alzheimer's Disease*, 68(1), 187–196. <https://doi.org/10.3233/JAD-180965>
- den Haan, J., Morrema, T. H. J., Verbraak, F. D., de Boer, J. F., Scheltens, P., Rozemuller, A. J., Bergen, A. A. B., Bouwman, F. H., & Hoozemans, J. J. (2018). Amyloid-beta and phosphorylated tau in post-mortem Alzheimer's disease retinas. *Acta Neuropathologica Communications*, 6(1), 147. <https://doi.org/10.1186/s40478-018-0650-x>
- Do, K. V., Kautzmann, M. I., Jun, B., Gordon, W. C., Nshimiyimana, R., Yang, R., & Bazan, N. G. (2019). Elovans counteract oligomeric beta-amyloid-induced gene expression and protect photoreceptors. *Proceedings of the National Academy of Sciences USA*, 116(48), 24317–24325. <https://doi.org/10.1073/pnas.1912959116>
- Doustar, J., Torbati, T., Black, K. L., Koronyo, Y., & Koronyo-Hamaoui, M. (2017). Optical coherence tomography in Alzheimer's disease and other neurodegenerative diseases. *Frontiers in Neurology*, 8, 701. <https://doi.org/10.3389/fneur.2017.00701>
- El Khoury, J., Toft, M., Hickman, S. E., Means, T. K., Terada, K., Geula, C., & Luster, A. D. (2007). Ccr2 deficiency impairs microglial accumulation and accelerates progression of Alzheimer-like disease. *Nature Medicine*, 13(4), 432–438. <https://doi.org/10.1038/nm1555>
- Ferreira, S. T., Lourenco, M. V., Oliveira, M. M., & De Felice, F. G. (2015). Soluble amyloid-beta oligomers as synaptotoxins leading to cognitive impairment in Alzheimer's disease. *Frontiers in Cellular Neuroscience*, 9, 191. <https://doi.org/10.3389/fncel.2015.00191>
- Ferretti, M. T., Merlini, M., Späni, C., Gericke, C., Schweizer, N., Enzmann, G., Engelhardt, B., Kulic, L., Suter, T., & Nitsch, R. M. (2016). T-cell brain infiltration and immature antigen-presenting cells in transgenic models of Alzheimer's disease-like cerebral amyloidosis. *Brain, Behavior, and Immunity*, 54, 211–225. <https://doi.org/10.1016/j.bbi.2016.02.009>
- Frenkel, D., Maron, R., Burt, D. S., & Weiner, H. L. (2005). Nasal vaccination with a proteosome-based adjuvant and glatiramer acetate clears  $\beta$ -amyloid in a mouse model of Alzheimer disease. *The Journal of Clinical Investigation*, 115(9), 2423–2433. <https://doi.org/10.1172/JCI23241>
- Gate, D., Saligrama, N., Leventhal, O., Yang, A. C., Unger, M. S., Middeldorp, J., Chen, K., Lehallier, B., Channappa, D., De Los Santos, M. B., McBride, A., Pluvinage, J., Elahi, F., Tam, G.-Y., Kim, Y., Greicius, M., Wagner, A. D., Aigner, L., Galasko, D. R., ... Wyss-Coray, T. (2020). Clonally expanded CD8 T cells patrol the cerebrospinal fluid in Alzheimer's disease. *Nature*, 577(7790), 399–404. <https://doi.org/10.1038/s41586-019-1895-7>
- Grimaldi, A., Brighi, C., Peruzzi, G., Ragozzino, D., Bonanni, V., Limatola, C., Ruocco, G., & Di Angelantonio, S. (2018). Inflammation, neurodegeneration and protein aggregation in the retina as ocular biomarkers for Alzheimer's disease in the 3xTg-AD mouse model. *Cell Death & Disease*, 9(6), 685. <https://doi.org/10.1038/s41419-018-0740-5>
- Gurney, R., Davidson, Y. S., Robinson, A. C., Richardson, A., Jones, M., Snowden, J. S., & Mann, D. M. A. (2018). Lysosomes, autophagosomes and Alzheimer pathology in dementia with Lewy body disease. *Neuropathology*, 38, 347–360. <https://doi.org/10.1111/neup.12472>
- Hadoux, X., Hui, F., Lim, J. K. H., Masters, C. L., Pébay, A., Chevalier, S., Ha, J., Loi, S., Fowler, C. J., Rowe, C., Villemagne, V. L., Taylor, E. N., Fluke, C., Soucy, J.-P., Lesage, F., Sylvestre, J.-P., Rosa-Neto, P., Mathotaarachchi, S., Gauthier, S., ... van Wijngaarden, P. (2019). Non-invasive in vivo hyperspectral imaging of the retina for potential biomarker use in Alzheimer's disease. *Nature Communications*, 10(1), 4227. <https://doi.org/10.1038/s41467-019-12242-1>



- Hempel, H., Toschi, N., Babiloni, C., Baldacci, F., Black, K. L., Bokde, A. L. W., & Lista, S. (2018). Revolution of Alzheimer Precision Neurology. Passageway of systems biology and neurophysiology. *Journal of Alzheimer's Disease*, 64(s1), S47–S105. <https://doi.org/10.3233/jad-179932>
- Hardy, J., Duff, K., Hardy, K. G., Perez-Tur, J., & Hutton, M. (1998). Genetic dissection of Alzheimer's disease and related dementias: Amyloid and its relationship to tau. *Nature Neuroscience*, 1(5), 355–358. <https://doi.org/10.1038/1565>
- Hart, N. J., Koronyo, Y., Black, K. L., & Koronyo-Hamaoui, M. (2016). Ocular indicators of Alzheimer's: exploring disease in the retina. *Acta Neuropathologica*, 132(6), 767–787. <https://doi.org/10.1007/s00401-016-1613-6>
- Hecht, M., Kramer, L. M., von Arnim, C. A. F., Otto, M., & Thal, D. R. (2018). Capillary cerebral amyloid angiopathy in Alzheimer's disease: Association with allocortical/hippocampal microinfarcts and cognitive decline. *Acta Neuropathologica*, 135(5), 681–694. <https://doi.org/10.1007/s00401-018-1834-y>
- Heneka, M. T., Carson, M. J., Khoury, J. E., Landreth, G. E., Brosseron, F., Feinstein, D. L., Jacobs, A. H., Wyss-Coray, T., Vitorica, J., Ransohoff, R. M., Herrup, K., Frautschy, S. A., Finsen, B., Brown, G. C., Verkhratsky, A., Yamanaka, K., Koistinaho, J., Latz, E., Halle, A., ... Kummer, M. P. (2015). Neuroinflammation in Alzheimer's disease. *The Lancet Neurology*, 14(4), 388–405. [https://doi.org/10.1016/S1474-4422\(15\)70016-5](https://doi.org/10.1016/S1474-4422(15)70016-5)
- Huang, P., Sun, J., Wang, F., Luo, X., Feng, J., Gu, Q., Liu, T. E., & Sun, X. (2017). MicroRNA expression patterns involved in amyloid beta-induced retinal degeneration. *Investigative Ophthalmology & Visual Science*, 58(3), 1726–1735. <https://doi.org/10.1167/iovs.16-20043>
- Huang, S., Tong, H., Lei, M., Zhou, M., Guo, W., Li, G., & Xu, P. (2018). Astrocytic glutamatergic transporters are involved in Abeta-induced synaptic dysfunction. *Brain Research*, 1678, 129–137. <https://doi.org/10.1016/j.brainres.2017.10.011>
- Hwang, Y. H., Song, M., Kim, Y. Y., Yeom, D. J., & Lee, J. H. (2014). Interocular symmetry of retinal nerve fibre layer thickness in healthy eyes: A spectral-domain optical coherence tomographic study. *Clinical and Experimental Optometry*, 97(6), 550–554. <https://doi.org/10.1111/cxo.12218>
- Jankowsky, J. L., Slunt, H. H., Gonzales, V., Jenkins, N. A., Copeland, N. G., & Borchelt, D. R. (2004). APP processing and amyloid deposition in mice haplo-insufficient for presenilin 1. *Neurobiology of Aging*, 25(7), 885–892. <https://doi.org/10.1016/j.neurobiolaging.2003.09.008>
- Jevtic, S., Sengar, A. S., Salter, M. W., & McLaurin, J. (2017). The role of the immune system in Alzheimer disease: Etiology and treatment. *Ageing Research Reviews*, 40, 84–94. <https://doi.org/10.1016/j.arr.2017.08.005>
- Ju, Y.-E., McLeland, J. S., Toedebusch, C. D., Xiong, C., Fagan, A. M., Duntley, S. P., Morris, J. C., & Holtzman, D. M. (2013). Sleep quality and preclinical Alzheimer disease. *JAMA Neurology*, 70(5), 587–593. <https://doi.org/10.1001/jamaneurol.2013.2334>
- Kayed, R., Head, E., Thompson, J. L., McIntire, T. M., Milton, S. C., Cotman, C. W., & Glabe, C. G. (2003). Common structure of soluble amyloid oligomers implies common mechanism of pathogenesis. *Science*, 300(5618), 486–489. <https://doi.org/10.1126/science.1079469>
- Kimbrough, I. F., Robel, S., Roberson, E. D., & Sontheimer, H. (2015). Vascular amyloidosis impairs the gliovascular unit in a mouse model of Alzheimer's disease. *Brain*, 138(Pt 12), 3716–3733. <https://doi.org/10.1093/brain/awv327>
- Koffie, R. M., Meyer-Luehmann, M., Hashimoto, T., Adams, K. W., Mielke, M. L., Garcia-Alloza, M., & Spires-Jones, T. L. (2009). Oligomeric amyloid  $\beta$  associates with postsynaptic densities and correlates with excitatory synapse loss near senile plaques. *Proceedings of the National Academy of Sciences*, 106(10), 4012–4017. <https://doi.org/10.1073/pnas.0811698106>
- Koronyo, Y., Biggs, D., Barron, E., Boyer, D. S., Pearlman, J. A., Au, W. J., Kile, S. J., Blanco, A., Fuchs, D.-T., Ashfaq, A., Frautschy, S., Cole, G. M., Miller, C. A., Hinton, D. R., Verdooner, S. R., Black, K. L., & Koronyo-Hamaoui, M. (2017). Retinal amyloid pathology and proof-of-concept imaging trial in Alzheimer's disease. *JCI Insight*, 2(16), 1–19. <https://doi.org/10.1172/jci.insight.93621>
- Koronyo, Y., Salumbides, B. C., Black, K. L., & Koronyo-Hamaoui, M. (2012). Alzheimer's disease in the retina: Imaging retinal abeta plaques for early diagnosis and therapy assessment. *Neuro-Degenerative Diseases*, 10(1–4), 285–293. <https://doi.org/10.1159/000335154>
- Koronyo, Y., Salumbides, B. C., Sheyn, J., Pelissier, L., Li, S., Ljubimov, V., & Koronyo-Hamaoui, M. (2015). Therapeutic effects of glatiramer acetate and grafted CD115(+) monocytes in a mouse model of Alzheimer's disease. *Brain*, 138(Pt 8), 2399–2422. <https://doi.org/10.1093/brain/awv150>
- Koronyo-Hamaoui, M., Ko, M. H. K., Koronyo, Y., Azoulay, D., Seksenyan, A., Kunis, G., Pham, M., Bakhsheshian, J., Rogeri, P., Black, K. L., Farkas, D. L., & Schwartz, M. (2009). Attenuation of AD-like neuropathology by harnessing peripheral immune cells: Local elevation of IL-10 and MMP-9. *Journal of Neurochemistry*, 111(6), 1409–1424. <https://doi.org/10.1111/j.1471-4159.2009.06402.x>
- Koronyo-Hamaoui, M., Koronyo, Y., Ljubimov, A. V., Miller, C. A., Ko, M. H. K., Black, K. L., Schwartz, M., & Farkas, D. L. (2011). Identification of amyloid plaques in retinas from Alzheimer's patients and noninvasive in vivo optical imaging of retinal plaques in a mouse model. *NeuroImage*, 54(Suppl. 1), S204–S217.
- Koronyo-Hamaoui, M., Shah, K., Koronyo, Y., Bernstein, E., Giani, J. F., Janjulia, T., Black, K. L., Shi, P. D., Gonzalez-Villalobos, R. A., Fuchs, S., Shen, X. Z., & Bernstein, K. E. (2014). ACE overexpression in myelomonocytic cells: effect on a mouse model of Alzheimer's disease. *Current Hypertension Reports*, 16(7), 444. <https://doi.org/10.1007/s11906-014-0444-x>
- Koronyo-Hamaoui, M., Sheyn, J., Hayden, E. Y., Li, S., Fuchs, D.-T., Regis, G. C., Lopes, D. H. J., Black, K. L., Bernstein, K. E., Teplow, D. B., Fuchs, S., Koronyo, Y., & Rentsendorj, A. (2020). Peripherally derived angiotensin converting enzyme-enhanced macrophages alleviate Alzheimer-related disease. *Brain*, 143(1), 336–358. <https://doi.org/10.1093/brain/awz364>
- Kuperstein, I., Broersen, K., Benilova, I., Rozenski, J., Jonckheere, W., Debulpaep, M., & De Strooper, B. (2010). Neurotoxicity of Alzheimer's disease A $\beta$  peptides is induced by small changes in the A $\beta$ 42 to A $\beta$ 40 ratio. *EMBO Journal*, 29(19), 3408–3420. <https://doi.org/10.1038/emboj.2010.211>
- Kusne, Y., Wolf, A. B., Townley, K., Conway, M., & Peyman, G. A. (2017). Visual system manifestations of Alzheimer's disease. *Acta Ophthalmologica*, 95(8), e668–e676. <https://doi.org/10.1111/aos.13319>
- La Morgia, C., Ross-Cisneros, F. N., Koronyo, Y., Hannibal, J., Gallassi, R., Cantalupo, G., Sambati, L., Pan, B. X., Tozer, K. R., Barboni, P., Provini, F., Avanzini, P., Carbonelli, M., Pelosi, A., Chui, H., Liguori, R., Baruzzi, A., Koronyo-Hamaoui, M., Sadun, A. A., & Carelli, V. (2016). Melanopsin retinal ganglion cell loss in Alzheimer disease. *Annals of Neurology*, 79(1), 90–109. <https://doi.org/10.1002/ana.24548>
- Lambert, M. P., Barlow, A. K., Chromy, B. A., Edwards, C., Freed, R., Liosatos, M., & Klein, W. L. (1998). Diffusible, nonfibrillar ligands derived from A $\beta$ <sub>1–42</sub> are potent central nervous system neurotoxins. *Proceedings of the National Academy of Sciences*, 95(11), 6448–6453. <https://doi.org/10.1073/pnas.95.11.6448>
- Lebson, L., Nash, K., Kamath, S., Herber, D., Carty, N., Lee, D. C., Li, Q., Szekeres, K., Jinwal, U., Koren, J., Dickey, C. A., Gottschall, P. E., Morgan, D., & Gordon, M. N. (2010). Trafficking CD11b-positive blood cells deliver therapeutic genes to the brain of amyloid-depositing



- transgenic mice. *The Journal of Neuroscience*, 30(29), 9651–9658. <https://doi.org/10.1523/jneurosci.0329-10.2010>
- Lehmann, M., Ghosh, P. M., Madison, C., Laforce, R., Corbetta-Rastelli, C., Weiner, M. W., Greicius, M. D., Seeley, W. W., Gorno-Tempini, M. L., Rosen, H. J., Miller, B. L., Jagust, W. J., & Rabinovici, G. D. (2013). Diverging patterns of amyloid deposition and hypometabolism in clinical variants of probable Alzheimer's disease. *Brain*, 136(Pt 3), 844–858. <https://doi.org/10.1093/brain/aws327>
- Lei, C., Lin, R., Wang, J., Tao, L., Fu, X., Qiu, Y., & Lei, B. (2017). Amelioration of amyloid beta-induced retinal inflammatory responses by a LXR agonist TO901317 is associated with inhibition of the NF-kappaB signaling and NLRP3 inflammasome. *Neuroscience*, 360, 48–60. <https://doi.org/10.1016/j.neuroscience.2017.07.053>
- Li, S., Hayden, E. Y., Garcia, V. J., Fuchs, D. T., Sheyn, J., Daley, D. A., & Koronyo-Hamaoui, M. (2020). Activated bone marrow-derived macrophages eradicate Alzheimer's-related Abeta42 oligomers and protect synapses. *Frontiers in Immunology*, 11, 49. <https://doi.org/10.3389/fimmu.2020.00049>
- Liesz, A. (2019). The vascular side of Alzheimer's disease. *Science*, 365(6450), 223–224. <https://doi.org/10.1126/science.aay2720>
- Liu, B., Rasool, S., Yang, Z., Glabe, C. G., Schreiber, S. S., Ge, J., & Tan, Z. (2009). Amyloid-peptide vaccinations reduce [beta]-amyloid plaques but exacerbate vascular deposition and inflammation in the retina of Alzheimer's transgenic mice. *American Journal of Pathology*, 175(5), 2099–2110.
- Liu, C.-Y., Yang, Y., Ju, W.-N., Wang, X., & Zhang, H.-L. (2018). Emerging roles of astrocytes in neuro-vascular unit and the tripartite synapse with emphasis on reactive gliosis in the context of Alzheimer's disease. *Frontiers in Cellular Neuroscience*, 12, 193. <https://doi.org/10.3389/fncel.2018.00193>
- Long, X., Zhang, L., Liao, W., Jiang, C., Qiu, B., & Alzheimer's Disease Neuroimaging Initiative. (2013). Distinct laterality alterations distinguish mild cognitive impairment and Alzheimer's disease from healthy aging: Statistical parametric mapping with high resolution MRI. *Human Brain Mapping*, 34(12), 3400–3410. <https://doi.org/10.1002/hbm.22157>
- Mahajan, D., & Votruba, M. (2017). Can the retina be used to diagnose and plot the progression of Alzheimer's disease? *Acta Ophthalmologica*, 95(8), 768–777. <https://doi.org/10.1111/aos.13472>
- Martens, R., Permanyer, M., Werth, K., Yu, K., Braun, A., Halle, O., Halle, S., Patzer, G. E., Bošnjak, B., Kiefer, F., Janssen, A., Friedrichsen, M., Poetzsch, J., Kohli, K., Lueder, Y., Gutierrez Jauregui, R., Eckert, N., Worbs, T., Galla, M., & Förster, R. (2020). Efficient homing of T cells via afferent lymphatics requires mechanical arrest and integrin-supported chemokine guidance. *Nature Communications*, 11(1), 1114. <https://doi.org/10.1038/s41467-020-14921-w>
- McLean, C. A., Cherny, R. A., Fraser, F. W., Fuller, S. J., Smith, M. J., Beyreuther, K., & Masters, C. L. (1999). Soluble pool of Abeta amyloid as a determinant of severity of neurodegeneration in Alzheimer's disease. *Annals of Neurology*, 46(6), 860–866.
- Mesulam, M. M., Weintraub, S., Rogalski, E. J., Wieneke, C., Geula, C., & Bigio, E. H. (2014). Asymmetry and heterogeneity of Alzheimer's and frontotemporal pathology in primary progressive aphasia. *Brain*, 137(Pt 4), 1176–1192. <https://doi.org/10.1093/brain/awu024>
- Meyer-Luehmann, M., Spires-Jones, T. L., Prada, C., Garcia-Alloza, M., de Calignon, A., Rozkalne, A., & Hyman, B. T. (2008). Rapid appearance and local toxicity of amyloid-beta plaques in a mouse model of Alzheimer's disease. *Nature*, 451(7179), 720–724. <https://doi.org/10.1038/nature06616>
- Michaud, J. P., Bellavance, M. A., Prefontaine, P., & Rivest, S. (2013). Real-time in vivo imaging reveals the ability of monocytes to clear vascular amyloid beta. *Cell Reports*, 5(3), 646–653. <https://doi.org/10.1016/j.celrep.2013.10.010>
- Minkova, L., Habich, A., Peter, J., Kaller, C. P., Eickhoff, S. B., & Kloppel, S. (2017). Gray matter asymmetries in aging and neurodegeneration: A review and meta-analysis. *Human Brain Mapping*, 38(12), 5890–5904. <https://doi.org/10.1002/hbm.23772>
- Nation, D. A., Sweeney, M. D., Montagne, A., Sagare, A. P., D'Orazio, L. M., Pachicano, M., Sepehrband, F., Nelson, A. R., Buennagel, D. P., Harrington, M. G., Benzinger, T. L. S., Fagan, A. M., Ringman, J. M., Schneider, L. S., Morris, J. C., Chui, H. C., Law, M., Toga, A. W., & Zlokovic, B. V. (2019). Blood-brain barrier breakdown is an early biomarker of human cognitive dysfunction. *Nature Medicine*, 25(2), 270–276. <https://doi.org/10.1038/s41591-018-0297-y>
- Ning, A., Cui, J., To, E., Ashe, K. H., & Matsubara, J. (2008). Amyloid-beta deposits lead to retinal degeneration in a mouse model of Alzheimer disease. *Investigative Ophthalmology & Visual Science*, 49(11), 5136–5143.
- O'Bryhim, B., Apte, R. S., Kung, N., Coble, D., & Van Stavern, G. P. (2018). Association of preclinical alzheimer disease with optical coherence tomographic angiography findings. *JAMA Ophthalmology*, 136(11), 1242–1248. <https://doi.org/10.1001/jamaophthalmol.2018.3556>
- Ortinski, P. I., Dong, J., Mungenast, A., Yue, C., Takano, H., Watson, D. J., Haydon, P. G., & Coulter, D. A. (2010). Selective induction of astrocytic gliosis generates deficits in neuronal inhibition. *Nature Neuroscience*, 13(5), 584–591. <https://doi.org/10.1038/nn.2535>
- Osborn, L. M., Kamphuis, W., Wadman, W. J., & Hol, E. M. (2016). Astroglial: An integral player in the pathogenesis of Alzheimer's disease. *Progress in Neurobiology*, 144, 121–141. <https://doi.org/10.1016/j.pneurobio.2016.01.001>
- Parthasarathy, R., Chow, K. M., Derafshi, Z., Fautsch, M. P., Hetling, J. R., Rodgers, D. W., & Pepperberg, D. R. (2015). Reduction of amyloid-beta levels in mouse eye tissues by intra-vitreally delivered neprilysin. *Experimental Eye Research*, 138, 134–144. <https://doi.org/10.1016/j.exer.2015.06.027>
- Pluvinage, J. V., & Wyss-Coray, T. (2020). Systemic factors as mediators of brain homeostasis, ageing and neurodegeneration. *Nature Reviews Neuroscience*, 21(2), 93–102. <https://doi.org/10.1038/s41583-019-0255-9>
- Proebstl, D., Voisin, M.-B., Woodfin, A., Whiteford, J., D'Acquisto, F., Jones, G. E., Rowe, D., & Nourshargh, S. (2012). Pericytes support neutrophil subendothelial cell crawling and breaching of venular walls in vivo. *Journal of Experimental Medicine*, 209(6), 1219–1234. <https://doi.org/10.1084/jem.20111622>
- Querques, G., Borrelli, E., Sacconi, R., De Vitis, L., Leocani, L., Santangelo, R., Magnani, G., Comi, G., & Bandello, F. (2019). Functional and morphological changes of the retinal vessels in Alzheimer's disease and mild cognitive impairment. *Scientific Reports*, 9(1), 63. <https://doi.org/10.1038/s41598-018-37271-6>
- Rajendran, L., & Paolicelli, R. C. (2018). Microglia-mediated synapse loss in Alzheimer's disease. *Journal of Neuroscience*, 38(12), 2911–2919. <https://doi.org/10.1523/JNEUROSCI.1136-17.2017>
- Ramanathan, A., Nelson, A. R., Sagare, A. P., & Zlokovic, B. V. (2015). Impaired vascular-mediated clearance of brain amyloid beta in Alzheimer's disease: The role, regulation and restoration of LRP1. *Frontiers in Aging Neuroscience*, 7, 136. <https://doi.org/10.3389/fnagi.2015.00136>
- Raskatov, J. A. (2019). What is the "Relevant" amyloid beta42 concentration? *ChemBioChem*, 20(13), 1725–1726. <https://doi.org/10.1002/cbic.201900097>
- Rasmussen, J., Mahler, J., Beschorner, N., Kaeser, S. A., Häslér, L. M., Baumann, F., Nyström, S., Portelius, E., Blennow, K., Lashley, T., Fox, N. C., Sepulveda-Falla, D., Glatzel, M., Oblak, A. L., Ghetti, B., Nilsson, K. P. R., Hammarström, P., Staufenbiel, M., Walker, L. C., & Jucker, M. (2017). Amyloid polymorphisms constitute distinct clouds of conformational variants in different etiological subtypes of Alzheimer's disease. *Proceedings of the National Academy of Sciences*, 114(49), 13018–13023. <https://doi.org/10.1073/pnas.1713215114>



- Rembach, A., Watt, A. D., Wilson, W. J., Villemagne, V. L., Burnham, S. C., Ellis, K. A., & Doecke, J. D. (2014). Plasma amyloid-beta levels are significantly associated with a transition toward Alzheimer's disease as measured by cognitive decline and change in neocortical amyloid burden. *Journal of Alzheimer's Disease*, *40*(1), 95–104. <https://doi.org/10.3233/jad-131802>
- Rentsendorj, A., Sheyn, J., Fuchs, D. T., Daley, D., Salumbides, B. C., Schubloom, H. E., & Koronyo-Hamaoui, M. (2018). A novel role for osteopontin in macrophage-mediated amyloid-beta clearance in Alzheimer's models. *Brain, Behavior, and Immunity*, *67*, 163–180. <https://doi.org/10.1016/j.bbi.2017.08.019>
- Rodriguez-Arellano, J. J., Parpura, V., Zorec, R., & Verkhratsky, A. (2016). Astrocytes in physiological aging and Alzheimer's disease. *Neuroscience*, *323*, 170–182. <https://doi.org/10.1016/j.neurosci.2015.01.007>
- Rosenzweig, N., Dvir-Szternfeld, R., Tsitsou-Kampeli, A., Keren-Shaul, H., Ben-Yehuda, H., Weill-Raynal, P., Cahalon, L., Kertser, A., Baruch, K., Amit, I., Weiner, A., & Schwartz, M. (2019). PD-1/PD-L1 checkpoint blockade harnesses monocyte-derived macrophages to combat cognitive impairment in a tauopathy mouse model. *Nature Communications*, *10*(1), 465. <https://doi.org/10.1038/s41467-019-08352-5>
- Rudy, C. C., Hunsberger, H. C., Weitzner, D. S., & Reed, M. N. (2015). The role of the tripartite glutamatergic synapse in the pathophysiology of Alzheimer's disease. *Aging and Disease*, *6*(2), 131–148. <https://doi.org/10.14336/ad.2014.0423>
- Schindler, S. E., Bollinger, J. G., Ovod, V., Mawuenyega, K. G., Li, Y., Gordon, B. A., Holtzman, D. M., Morris, J. C., Benzinger, T. L. S., Xiong, C., Fagan, A. M., & Bateman, R. J. (2019). High-precision plasma  $\beta$ -amyloid 42/40 predicts current and future brain amyloidosis. *Neurology*, *93*(17), e1647–e1659. <https://doi.org/10.1212/wnl.00000000000008081>
- Schön, C., Hoffmann, N. A., Ochs, S. M., Burgold, S., Filser, S., Steinbach, S., Seeliger, M. W., Arzberger, T., Goedert, M., Kretschmar, H. A., Schmidt, B., & Herms, J. (2012). Long-term in vivo imaging of fibrillar tau in the retina of P301S transgenic mice. *PLoS One*, *7*(12), e53547.
- Schultz, N., Brannstrom, K., Byman, E., Moussaud, S., Nielsen, H. M., Netherlands Brain, B., & Wennstrom, M. (2018). Amyloid-beta 1–40 is associated with alterations in NG2+ pericyte population ex vivo and in vitro. *Aging Cell*, *17*(3), e12728. <https://doi.org/10.1111/accel.12728>
- Schultz, N., Byman, E., Netherlands Brain, B., & Wennstrom, M. (2020). Levels of retinal amyloid-beta correlate with levels of retinal IAPP and hippocampal amyloid-beta in neuropathologically evaluated individuals. *Journal of Alzheimer's Disease*, *73*(3), 1201–1209. <https://doi.org/10.3233/JAD-190868>
- Selkoe, D. J. (2008). Soluble oligomers of the amyloid beta-protein impair synaptic plasticity and behavior. *Behavioral Brain Research*, *192*(1), 106–113. <https://doi.org/10.1016/j.bbr.2008.02.016>
- Shankar, G. M., Li, S., Mehta, T. H., Garcia-Munoz, A., Shepardson, N. E., Smith, I., & Selkoe, D. J. (2008). Amyloid-beta protein dimers isolated directly from Alzheimer's brains impair synaptic plasticity and memory. *Nature Medicine*, *14*(8), 837–842. <https://doi.org/10.1038/nm1782>
- Shi, H., Koronyo, Y., Rentsendorj, A., Regis, G. C., Sheyn, J., Fuchs, D.-T., Kramerov, A. A., Ljubimov, A. V., Dumitrascu, O. M., Rodriguez, A. R., Barron, E., Hinton, D. R., Black, K. L., Miller, C. A., Mirzaei, N., & Koronyo-Hamaoui, M. (2020). Identification of early pericyte loss and vascular amyloidosis in Alzheimer's disease retina. *Acta Neuropathologica*, *139*(5), 813–836. <https://doi.org/10.1007/s00401-020-02134-w>
- Sidiqi, A., Wahl, D., Lee, S., Ma, D. A., To, E., Cui, J., To, E., Beg, M. F., Sarunic, M., & Matsubara, J. A. (2020). In vivo retinal fluorescence imaging with curcumin in an Alzheimer mouse model. *Frontiers in Neuroscience*, *14*, 713. <https://doi.org/10.3389/fnins.2020.00713>
- Simard, A. R., Soulet, D., Gowing, G., Julien, J. P., & Rivest, S. (2006). Bone marrow-derived microglia play a critical role in restricting senile plaque formation in Alzheimer's disease. *Neuron*, *49*(4), 489–502. <https://doi.org/10.1016/j.neuron.2006.01.022>
- Son, H., Kim, S., Jung, D.-H., Baek, J. H., Lee, D. H., Roh, G. S., Kang, S. S., Cho, G. J., Choi, W. S., Lee, D. K., & Kim, H. J. (2019). Insufficient glutamine synthetase activity during synaptogenesis causes spatial memory impairment in adult mice. *Scientific Reports*, *9*(1), 252. <https://doi.org/10.1038/s41598-018-36619-2>
- Sperling, R. A., Donohue, M. C., Raman, R., Sun, C.-K., Yaari, R., Holdridge, K., Siemers, E., Johnson, K. A., & Aisen, P. S. (2020). Association of factors with elevated amyloid burden in clinically normal older individuals. *JAMA Neurology*, *77*, 735. <https://doi.org/10.1001/jamaeurol.2020.0387>
- Sweeney, M. D., Sagare, A. P., & Zlokovic, B. V. (2018). Blood-brain barrier breakdown in Alzheimer disease and other neurodegenerative disorders. *Nature Reviews Neurology*, *14*(3), 133–150. <https://doi.org/10.1038/nrnneurol.2017.188>
- Tani, H., Dulla, C. G., Farzampour, Z., Taylor-Weiner, A., Huguenard, J. R., & Reimer, R. J. (2014). A local glutamate-glutamine cycle sustains synaptic excitatory transmitter release. *Neuron*, *81*(4), 888–900. <https://doi.org/10.1016/j.neuron.2013.12.026>
- Tetzloff, K. A., Graff-Radford, J., Martin, P. R., Tosakulwong, N., Machulda, M. M., Duffy, J. R., Clark, H. M., Senjem, M. L., Schwarz, C. G., Sychalla, A. J., Drubach, D. A., Jack, C. R., Lowe, V. J., Josephs, K. A., & Whitwell, J. L. (2018). Regional distribution, asymmetry, and clinical correlates of tau uptake on [18F]AV-1451 PET in atypical Alzheimer's disease. *Journal of Alzheimer's Disease*, *62*(4), 1713–1724. <https://doi.org/10.3233/jad-170740>
- Thal, D. R., Ghebremedhin, E., Rub, U., Yamaguchi, H., Del Tredici, K., & Braak, H. (2002). Two types of sporadic cerebral amyloid angiopathy. *Journal of Neuropathology and Experimental Neurology*, *61*(3), 282–293.
- Thal, D. R., Griffin, W. S., & Braak, H. (2008). Parenchymal and vascular A $\beta$ -deposition and its effects on the degeneration of neurons and cognition in Alzheimer's disease. *Journal of Cellular and Molecular Medicine*, *12*(5B), 1848–1862. <https://doi.org/10.1111/j.1582-4934.2008.00411.x>
- Thal, D. R., Griffin, W. S., de Vos, R. A., & Ghebremedhin, E. (2008). Cerebral amyloid angiopathy and its relationship to Alzheimer's disease. *Acta Neuropathologica*, *115*(6), 599–609. <https://doi.org/10.1007/s00401-008-0366-2>
- Toga, A. W., & Thompson, P. M. (2003). Mapping brain asymmetry. *Nature Reviews Neuroscience*, *4*(1), 37–48. <https://doi.org/10.1038/nn1009>
- Tsai, Y., Lu, B., Ljubimov, A. V., Girman, S., Ross-Cisneros, F. N., Sadun, A. A., Svendsen, C. N., Cohen, R. M., & Wang, S. (2014). Ocular changes in TgF344-AD rat model of Alzheimer's disease. *Investigative Ophthalmology & Visual Science*, *55*(1), 523–534. <https://doi.org/10.1167/iovs.13-12888>
- Verkhratsky, A., & Nedergaard, M. (2018). Physiology of astroglia. *Physiological Reviews*, *98*(1), 239–389. <https://doi.org/10.1152/physrev.00042.2016>
- Vilella, A., Belletti, D., Sauer, A. K., Hagemeyer, S., Sarowar, T., Masoni, M., Stasiak, N., Mulvihill, J. J. E., Ruozi, B., Forni, F., Vandelli, M. A., Tosi, G., Zoli, M., & Grabrucker, A. M. (2018). Reduced plaque size and inflammation in the APP23 mouse model for Alzheimer's disease after chronic application of polymeric nanoparticles for CNS targeted zinc delivery. *Journal of Trace Elements in Medicine and Biology*, *49*, 210–221. <https://doi.org/10.1016/j.jtemb.2017.12.006>
- Wachinger, C., Salat, D. H., Weiner, M., & Reuter, M. (2016). Whole-brain analysis reveals increased neuroanatomical asymmetries in dementia for hippocampus and amygdala. *Brain*, *139*(Pt 12), 3253–3266. <https://doi.org/10.1093/brain/aww243>





- Wahlund, L. O., Andersson-Lundman, G., Basun, H., Almkvist, O., Bjorksten, K. S., Saaf, J., & Wetterberg, L. (1993). Cognitive functions and brain structures: A quantitative study of CSF volumes on Alzheimer patients and healthy control subjects. *Magnetic Resonance Imaging*, 11(2), 169–174. [https://doi.org/10.1016/0730-725x\(93\)90021-5](https://doi.org/10.1016/0730-725x(93)90021-5)
- Walker, D. G., Lue, L. F., Tang, T. M., Adler, C. H., Caviness, J. N., Sabbagh, M. N., & Beach, T. G. (2017). Changes in CD200 and intercellular adhesion molecule-1 (ICAM-1) levels in brains of Lewy body disorder cases are associated with amounts of Alzheimer's pathology not alpha-synuclein pathology. *Neurobiology of Aging*, 54, 175–186. <https://doi.org/10.1016/j.neurobiolaging.2017.03.007>
- Wang, Y., Ulland, T. K., Ulrich, J. D., Song, W., Tzaferis, J. A., Hole, J. T., Yuan, P., Mahan, T. E., Shi, Y., Gilfillan, S., Cella, M., Grutzendler, J., DeMattos, R. B., Cirrito, J. R., Holtzman, D. M., & Colonna, M. (2016). TREM2-mediated early microglial response limits diffusion and toxicity of amyloid plaques. *The Journal of Experimental Medicine*, 213(5), 667–675. <https://doi.org/10.1084/jem.20151948>
- Weise, C. M., Chen, K., Chen, Y., Kuang, X., Savage, C. R., & Reiman, E. M. (2018). Left lateralized cerebral glucose metabolism declines in amyloid-beta positive persons with mild cognitive impairment. *NeuroImage Clinical*, 20, 286–296. <https://doi.org/10.1016/j.nicl.2018.07.016>
- Wyss-Coray, T., & Mucke, L. (2002). Inflammation in neurodegenerative disease—a double-edged sword. *Neuron*, 35(3), 419–432.
- Zlokovic, B. V. (2011). Neurovascular pathways to neurodegeneration in Alzheimer's disease and other disorders. *Nature Reviews Neuroscience*, 12(12), 723–738. <https://doi.org/10.1038/nrn3114>
- Zoia, C., Cogliati, T., Tagliabue, E., Cavaletti, G., Sala, G., Galimberti, G., Rivolta, I., Rossi, V., Frattola, L., & Ferrarese, C. (2004). Glutamate transporters in platelets: EAAT1 decrease in aging and in Alzheimer's disease. *Neurobiology of Aging*, 25(2), 149–157. [https://doi.org/10.1016/s0197-4580\(03\)00085-x](https://doi.org/10.1016/s0197-4580(03)00085-x)
- Zou, J., Wang, Y. X., Mu, H. J., Xiang, J., Wu, W., Zhang, B., & Xie, P. (2011). Down-regulation of glutamine synthetase enhances migration of rat astrocytes after in vitro injury. *Neurochemistry International*, 58(3), 404–413. <https://doi.org/10.1016/j.neuint.2010.12.018>
- Zuroff, L., Daley, D., Black, K. L., & Koronyo-Hamaoui, M. (2017). Clearance of cerebral Abeta in Alzheimer's disease: reassessing the role of microglia and monocytes. *Cellular and Molecular Life Sciences*, 74(12), 2167–2201. <https://doi.org/10.1007/s00018-017-2463-7>

## SUPPORTING INFORMATION

Additional supporting information may be found online in the Supporting Information section.

**How to cite this article:** Doustar J, Rentsendorj A, Torbati T, et al. Parallels between retinal and brain pathology and response to immunotherapy in old, late-stage Alzheimer's disease mouse models. *Aging Cell*. 2020;19:e13246. <https://doi.org/10.1111/acer.13246>